Universidade de São Paulo
Instituto de Física

Perfis de Emissividade no Tokamak TCABR

Alexandre Machado de Oliveira

Orientador: Prof. Dr. Zwinglio de Oliveira Guimarães Filho

Dissertação de mestrado apresentada ao Instituto de Física para a obtenção do título de Mestre em Ciências

Banca Examinadora:

Prof. Dr. Zwinglio de Oliveira Guimarães Filho – IFUSP
Prof. Dr. Iberê Luiz Caldas – IFUSP
Profa. Dra. Maria Célia Ramos de Andrade – INPE

São Paulo
2017

FICHA CATALOGRÁFICA
Preparada pelo Serviço de Biblioteca e Informação
do Instituto de Física da Universidade de São Paulo

Oliveira, Alexandre Machado de

Perfis de emissividade no Tokamak TCABR. São Paulo, 2017.

Dissertação (Mestrado) – Universidade de São Paulo. Instituto de Física. Depto. de Física Aplicada.

Orientador: Prof. Dr. Zwinglio de Oliveira Guimarães Filho
Área de Concentração: Física Aplicada

Unitermos: 1. Física de plasmas; 2. Tokamaks; 3. Radiação; 4. Física óptica; 5. Radon.

USP/IF/SBI-045/2017

University of São Paulo
Physics Institute

Emissivity Profiles at TCABR Tokamak

Alexandre Machado de Oliveira

Advisor: Prof. Dr. Zwinglio de Oliveira Guimarães Filho

Master Thesis submitted to Physics Institute
to obtain the Master of Science Degree

Examination Board:

Prof. Dr. Zwinglio de Oliveira Guimarães Filho – IFUSP
Prof. Dr. Iberê Luiz Caldas – IFUSP
Profa. Dra. Maria Célia Ramos de Andrade – INPE

São Paulo
2017

Este trabalho é dedicado a Maria Helena.

Agradecimentos

Agradeço imensamente ao Professor Zwinglio de Oliveira Guimarães Filho pela oportunidade proporcionada neste trabalho, por partilhar seu conhecimento, por sua excelente, dedicada, paciente e objetiva orientação, bem como por sua amizade.

Quero agradecer também aos Professores da área de Física de Plasmas: Ricardo M. O. Galvão, José Helder F. Severo, Ivan C. Nascimento, Artour Elfimov, Iberê L. Caldas, Dennis L. Toufen e Francisco E. M. da Silveira, pelos conhecimentos transmitidos.

Muito obrigado a todos os funcionários do Instituto de Física que compartilharam esse período comigo, em especial, a Sra. Eleonora D. V. Lo Duca e ao Sr. Nelson A. M. Cuevas.

Agradeço aos companheiros de jornada: Tiago Fernandes, Gilson Ronchi, Paulo G. P. P. Puglia, Tárcius N. Ramos, Gabriel M. Silva, Wilson A. H. Baquero, Diego S. Oliveira, Vinícius N. Duarte, Reneé J. F. Sgalla e Gustavo G. Grenfell por diversas discussões que enriqueceram minhas reflexões e contribuíram para o entendimento de muitas questões.

Expresso também um grande agradecimento à professora Maria Célia R. Andrade por seus comentários e sugestões de melhoria na finalização deste trabalho.

Um especial agradecimento a Maria Helena Gonçalves Rodrigues por seu constante incentivo, apoio, carinho, dedicação e inabalável confiança.

Finalmente, expresso meus profundos agradecimentos ao Amor Divino, por sempre nos perdoar, por nos permitir essa existência física por meio de nossas famílias e pela generosidade da vida por sempre colocar em meu caminho excelentes pessoas.

Muito Obrigado!

Resumo

A determinação dos perfis de equilíbrio do plasma é necessária para avaliar as propriedades do confinamento e para investigar os efeitos de perturbações. Diagnósticos ópticos podem ser usados para determinar alguns desses perfis. No entanto, esses diagnósticos medem toda a radiação luminosa emitida em um ângulo sólido que ilumina cada canal do detector através de uma fenda. Assim, a verdadeira grandeza física medida é a emissividade integrada ao longo da linha de visada. Com isso, algum procedimento de deconvolução, como a inversão de Abel, se faz necessário para obter o perfil de emissividade. No tokamak TCABR do Instituto de Física da USP, um bolômetro de 24 canais e um detector de raios-X moles de 20 canais são utilizados para medir a emissividade do plasma no intervalo de comprimento de onda de 1 a 1.000 nm, dependendo dos filtros utilizados. Neste trabalho, uma simulação numérica é usada para calcular o sinal medido pelos diagnósticos para um dado perfil de emissividade, possibilitando a comparação direta com os dados experimentais, evitando a realização da inversão de Abel e os problemas numéricos associados aos procedimentos de deconvolução. Pela consideração da geometria do tokamak TCABR, as coordenadas espaciais podem ser relacionadas com as coordenadas lineares normalizadas do plasma por meio da imposição de um modelo de emissividade para o plasma que dependa de alguns parâmetros livres, permitindo que a emissividade resultante em cada ponto possa ser calculada. Assim, a luminosidade de cada canal é calculada pela integral da emissividade modelada em cada linha de visada (Transformada de Radon). Os parâmetros livres dos perfis de emissividade são determinados ajustando-se as luminosidades calculadas em termos das luminosidades medidas. Nós consideramos três modelos de perfis de emissividade: um modelo parabólico em lei de potência, um modelo gaussiano e um modelo baseado em funções de Bessel. Observamos que o perfil parabólico ajusta-se bem aos dados do bolômetro, ao passo que o perfil gaussiano é adequado para descrever os dados obtidos com o detector de raios-X moles.

Palavras-chave: Física de Plasmas, Tokamaks, Radiação, Física Óptica, Radon.

Abstract

The determination of plasma equilibrium profiles is necessary to evaluate the properties of the confinement and to investigate perturbation effects. Optical diagnostics can be used to determine some of these profiles. However, these diagnostics measure all emitted radiation at a solid angle that illuminate each diagnostic channel through a slit. Therefore, the real measured quantity is the emissivity integrated along the line-of-sight and some unfolding procedure, like Abel's inversion, is commonly used to recover the emissivity profile. In TCABR tokamak, at the Physics Institute of the University of São Paulo, a 24-channel bolometer and a 20-channel soft X-ray optical diagnostics are used to measure the plasma emissivity in wavelength range from 1.0 to 1000 nm, depending on the used filters. In this work, a numerical simulation is used to compute the signal measured by the diagnostics for a given emissivity profile, allowing direct comparison with the experimental data and avoiding the use of the Abel's inversion directly and the numerical difficulties associated with unfolding procedures. By considering TCABR tokamak geometry, spatial coordinates can be related to the normalized linear coordinates of the plasma by imposing a plasma emissivity model that depends on some free parameters, allowing the emissivity resulting in each point can be calculated. Thus, the luminosity of each channel is calculated by the integral of the emissivity modeled in each line-of-sight (Radon Transformation). Emissivity model free parameters are determined by fitting calculated luminosity to measured one. We considered three types of emissivity profiles: a parabolic model in law of power, a Gaussian model and a model based on Bessel functions. We observed that the parabolic profile fits well the bolometer data, while the Gaussian profile is adequate to describe the data obtained with the soft X-ray detector.

Keywords: Plasma Physics, Tokamaks, Radiation, Optical Physics, Radon.

Contents

1. **Introduction**

Nowadays, nuclear fusion is being developed in order to reach feasible reactors that could produce energy in commercial scale. Tokamak machines will be used to produce plasma at hundreds of millions Celsius degrees, making deuterium-tritium (D-T) fusion possible. Due to its extremely high temperature, it is not trivial measuring plasma properties.

Many plasma diagnostics have been developed like reflectometers, interferometers, electron-cyclotron RF diagnostic and Thomson lasers scattering diagnostic. All of them are of high costing technology. However, there are some affordable electronic diagnostics that measure emitted radiation from near infrared band $(\sim 1eV)$ up to low energy x-rays band $(\sim 1keV)$ that are generically called optical detectors.

However, measurement process of optical diagnostics results in a sum of all points that emitted radiation towards the detector, inside its solid angle cone, while the relevant physical quantity is a local emissivity, not the line integrated one.

Therefore, there are some statistical difficulties inherent to the process of emissivity reconstruction due to this being an unfolding one [1, 2].

This work consists in an implementation of an emissivity reconstruction method for TCABR tokamak [3, 4, 5, 6] optical diagnostics. This method makes possible to estimate some plasma equilibrium parameters that are useful for describing the average optical emissivity in time intervals where plasma remains in quasi-stationary condition.

1.1. Tokamak Machine

Tokamak stands for Toroidal Chamber with Magnetic Coils. It is used to produce controlled plasma. A simple tokamak uses mainly three coil systems:

a) Toroidal coils, responsible for toroidal magnetic field inducement;
b) Primary coil, also known as ohmic heating system, responsible for gas ionization and plasma current inducement and control;
c) Position control coils, also known as vertical magnetic field, responsible for plasma positioning and plasma stability.

Hydrogen is often used, especially in small tokamaks, because its atoms have low ionization potential and the lowest possible inertia (mass).

In Figure 1-1, a tokamak current and magnetic fields schematic diagram is shown.

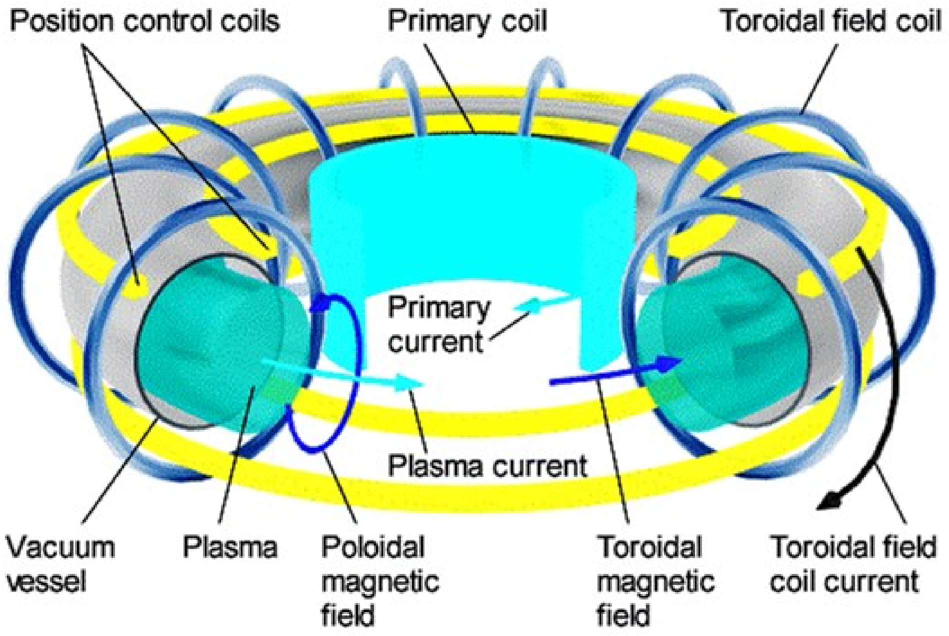

Figure 1-1: Tokamak Current and Magnetic Fields Schematic Diagram[1]

An important topic of tokamak plasma fusion research is to learn about plasma properties like confinement and impurities contamination quality. This knowledge is essential in order to achieve the required conditions for Deuterium-Tritium fusion process. In this context, experimental determination of the equilibrium plasma emission is important to properly describe and quantify plasma confinement.

1.2. TCABR Tokamak

TCABR stands for “Tokamak Chauffage Alfvén Brasilien” – Brazilian Alfvén Heating Tokamak. This machine came from Ecole Polytechnique Fédérale de Lausanne, Switzerland, in the mid 90’s. It was known as TCA at that time.

---

[1] Adapted from *Tokamaks,* <http://www.plasma.inpe.br/LAP_Portal/LAP_Site/Text/Tokamaks.htm>, not available anymore. Backup available at, *Tokamaks,* <http://www.sunist.org/shared_documents/SUNIST_Lab_Ceremony/00_introduction_to_ST/Fusion,_Tokamak_and_Spherical_Tokamak/Tokamaks.htm>, accessed in Jun 19, 2017.

TCABR Tokamak is at Plasma Physics Laboratory (Laboratório de Física de Plasmas) and belongs to Applied Physics Department, Physics Institute, University of São Paulo. It started operating in 1999, replacing the old TBR-1 Tokamak [7] that was built at this laboratory in the beginning of 80's.

Plasma Physics Laboratory is shown in Figure 1-2. TCABR Tokamak is at the central portion of the room.

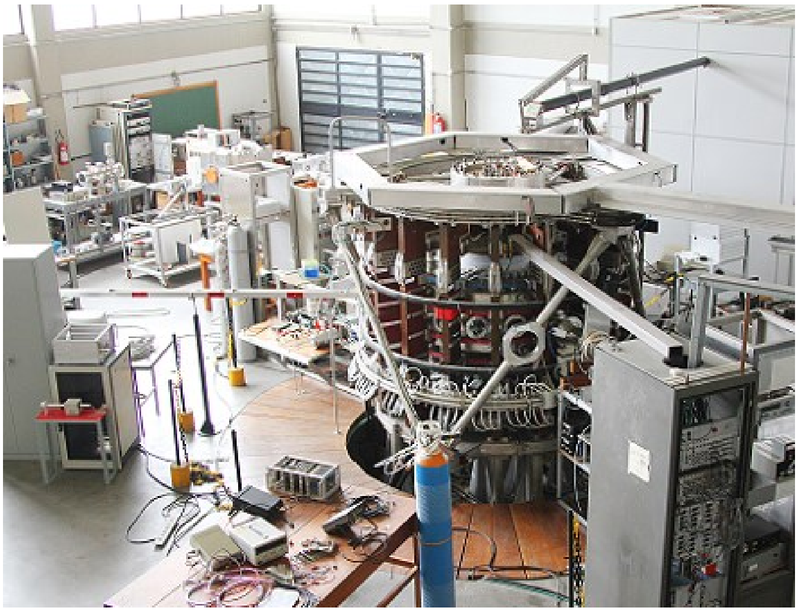

Figure 1-2: TCABR Tokamak at Plasma Physics Laboratory[2]

Considering just one linear dimension, TCABR is about three times TBR-1 size, which means that its plasma volume is approximately 30 times bigger. However, TCABR tokamak is considered to be a small size machine in the worldwide scenario.

Despite this, it represents an interesting tokamak size since some plasma disrupting experiments can be carried out in this machine without a significant permanent damage to the vacuum vessel. This is possible due to its relative low plasma total energy – low plasma volume, low temperature and low electron density in comparison to large machines. Table 1-1 shows TCABR Tokamak main parameters.

---

[2] Source: "Início - Departamento de Física Aplicada _ Departamento Física Aplicada", <http://portal.if.usp.br/fap/>, accessed in Jun 19, 2017.

TCABR Parameters	**Values**
Major Radius (R_0)	61.5 cm
Minor Radius (a)	18 cm
Plasma Current (I_p)	90 kA
Toroidal Magnetic Field (B_T)	$\sim 1.07 \text{ T}$
Line Average Electron Density ($\overline{n_e}$)	0.9 to 3.0 ($10^{19} m^{-3}$)
Central Electron Temperature (T_e)	$\sim 500 \text{ eV}$
Plasma Shape	Circular
Pulse Length	$\sim 100 \text{ ms}$

Table 1-1: TCABR Tokamak Main Parameters

More information about TCABR Tokamak can be found in reference [3] and at its official web page [8].

1.3. Typical Discharge

A typical TCABR tokamak discharge has four phases: loading primary coil, gas ionization with plasma current increase, current plateau and, finally, electron-ion recombination with plasma current decrease.

Loading primary coil is the first phase, when energy is transferred from capacitor banks to primary coil or ohmic heating system. It starts at 0 ms and lasts up to 28 ms since there is not any electron or ion in tokamak chamber, plasma current remains in zero. Around 13 to 14 ms, a spontaneous ionization occurs as a combination of induced loop voltage (V_{Loop}) level and gas pressure inside the tokamak chamber, working as a seed for main ionization in next phase.

Gas ionization and plasma current increase is the second phase. It starts at 28 ms, when capacitors bank is disconnected and replaced by a fixed resistance making loop voltage increases to a very high value, about 16 V. In this process, almost all gas inside the tokamak chamber is ionized. Plasma current starts increasing very fast because electrons and ions are accelerated by loop voltage. Around 30 ms, primary coil circuit changes again, forcing loop voltage to decrease to about 8 V in order to provide a more controlled plasma current increase.

Plasma current increases up to around 40 ms and reaches values of about 90 kA. In fact, plasma works as a secondary coil of an energy transformer.

Achieving a current plateau is the third phase of the discharge. It starts around 40 ms, when plasma current reaches its maximum value. In this phase, the plasma current is maintained as close as possible to the maximum value by switching the primary coil circuit, keeping primary current changing rates as constant as possible. This phase ends around 100 to 110 ms, depending on tokamak adjusts.

Electron-ion recombination with plasma current decrease is the fourth phase of the discharge. It starts when primary coil circuit cannot be switched anymore due to the fact that its energy is over. Plasma current falls down freely until instabilities make ion-electron recombination to occur abruptly. This phase starts around 100 to 110 ms and finishes around 140 to 160 ms, depending on tokamak adjusts.

Figure 1-3 shows typical TCABR tokamak discharge plasma current.

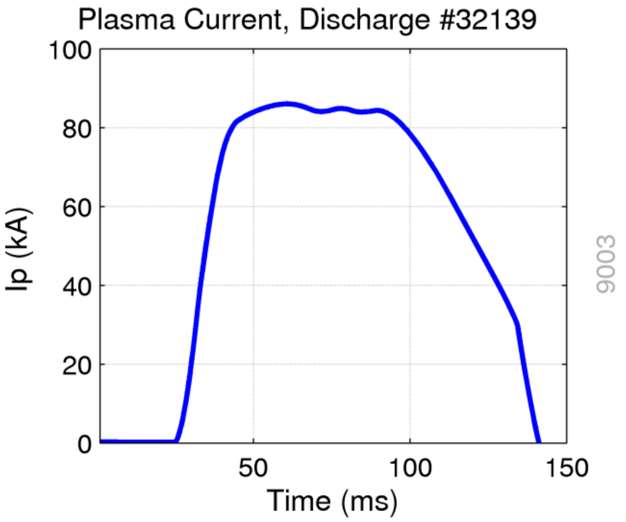

Figure 1-3: Typical TCABR Tokamak Discharge Plasma Current

Another important plasma parameter is its central electron density. In the conventional tokamak discharge, central electron density is mainly controlled by the gas injection. In this work, central electron density will be referred just as electron density.

Gas injection time profile is previously set by tokamak operator in order to reach some objectives during the discharge. Discharges are repeated and the system readjusted up to reach a scientific interesting condition.

In this work, plasma current and electron density were considered plasma control parameters for almost stationary condition characterization, in specific time intervals. In Figure

1-4 and Figure 1-5, both plasma control parameters are shown for a low density ($\sim 1.2\,.10^{19} m^{-3}$) discharge and for a high density ($\sim 2.0\,.10^{19} m^{-3}$) discharge, respectively.

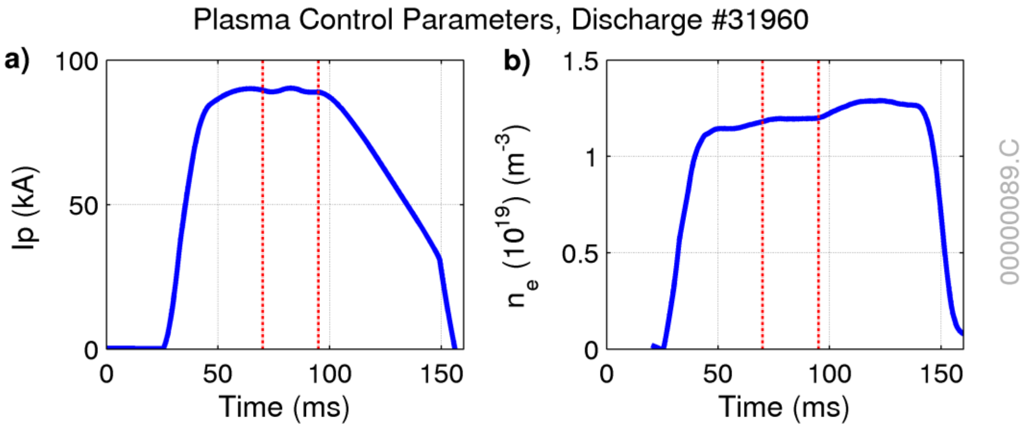

Figure 1-4: Plasma Control Parameters for Low Density Discharge #31960,

(a) Plasma Current, (b) Electron Density

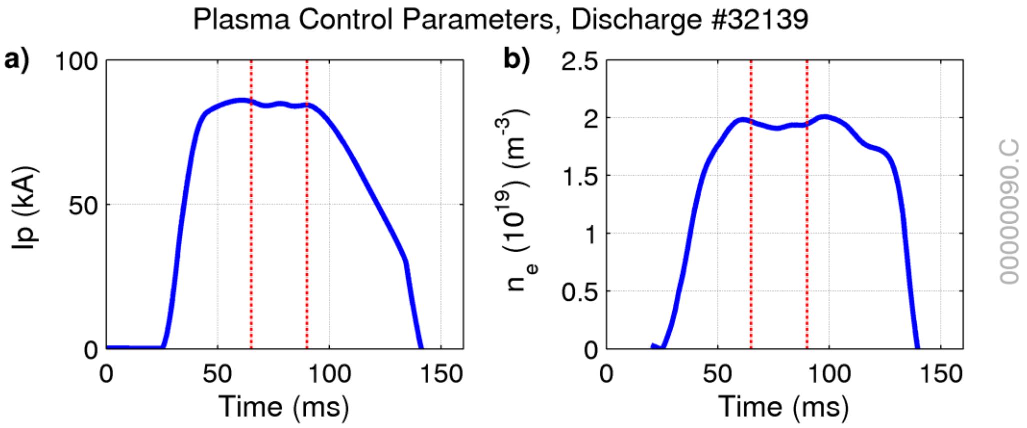

Figure 1-5: Plasma Control Parameters for High Density Discharge #32139,

(a) Plasma Current, (b) Electron Density

1.4. Plasma Equations

Plasma equations are subject of studies in MagnetoHydroDynamics (MHD) theory. These equations are derived from a set of electromagnetic, continuity and Newton equations plus Ohm’s law.

The study of these equations is not subject of this work. Therefore, only the equilibrium condition will be used, since this condition explains the existence of the plasma surfaces with constant plasma pressure.

1.4.1.Plasma Equilibrium

The plasma equilibrium conditions are obtained by setting all temporal dependences to zero, that is, by imposing that all time derivatives of the MHD equations are zero. In this case, MHD model shows that magnetic field strength keeps unchanged overall closed surfaces and pressure (p) is defined by equation 1-1.

$$\nabla p = \vec{J} \times \vec{B} \qquad 1\text{-}1$$

where:

$\vec{J}$ is the electric current density;

$\vec{B}$ is the total magnetic field, that is, the sum of poloidal and toroidal magnetic fields.

This equation implies that pressure gradient is perpendicular to both electric current density and magnetic field. Note that $\vec{J}$ and $\vec{B}$ are tangential to each pressure surface.

Considering TCABR Tokamak toroidal geometry, the simplest solution of equation 1-1 is a set of toroids over which their surfaces are at nearly constant pressure. Figure 1-6 shows an example for this kind of solution.

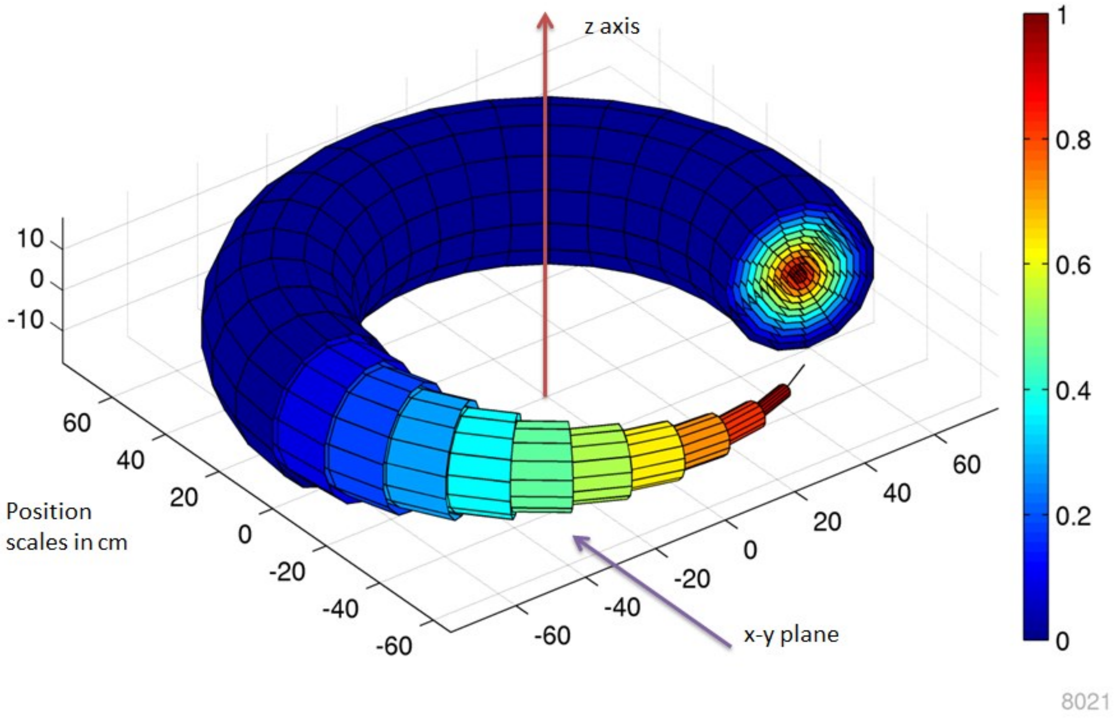

Figure 1-6: TCABR Plasma Toroidal Schematic View.

The plasma pressure in a generic unit is shown in color scale.

1.4.2.Coordinates Systems

A set of toroidal coordinates (r', θ, φ) can define any P point in plasma volume, for a given R_0, as shown by Figure 1-7.

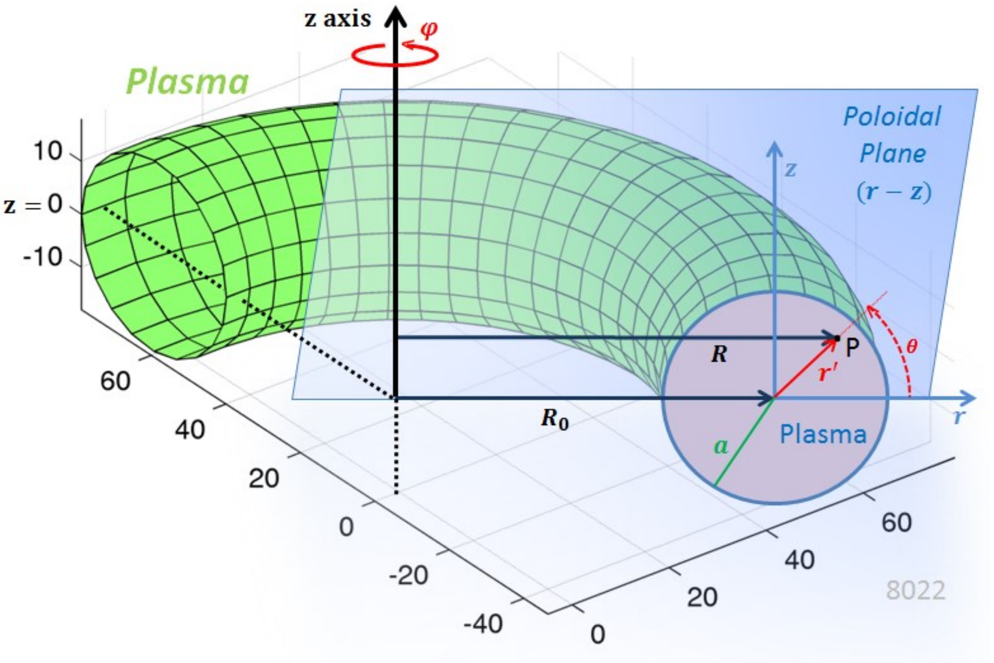

Figure 1-7: Toroidal and Poloidal Coordinates Systems

This work will use only specific poloidal planes related to Bolometer and Soft X-Rays diagnostics. For these cases, poloidal coordinates (r', θ) or Cartesian coordinates (r, z) can define any P point at the specific poloidal plane.

In order to simplify plasma emissivity calculations, it is defined a normalized coordinate ρ, given by equation 1-2, that is the ratio between the distance (r') of a P point to toroidal axis and the poloidal plasma radius (a).

$$\rho = \frac{|r'|}{a}\,, \quad 0 \leq \rho \leq 1 \qquad \text{1-2}$$

It is convenient to study a poloidal section [9] using polar coordinate system (ρ, θ) defined by a fixed toroidal position φ.

1.4.3.Profile Basic Equation

Usually, the plasma density, temperature and pressure profiles are well represented by the phenomenological model given by equation 1-3. This equation is a possible poloidal solution to the equation 1-1.

$$X(\rho) = X_0(1-\rho^2)^\gamma \tag{1-3}$$

where:

X_0 is the maximum value of the physical quantity described;

ρ is the normalized coordinate defined in equation 1-2;

γ is the exponent related to the described physical quantity.

Figure 1-8 shows an example plot for equation 1-3 and its poloidal view.

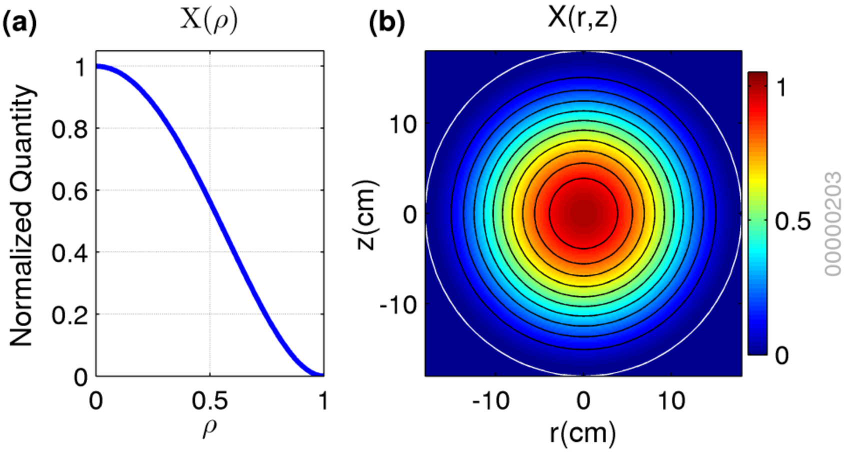

Figure 1-8: (a) Plot for Equation 1-3 where $X_0 = 1.0$ and $\gamma = 2$ and (b) Its Respective Poloidal View

Another important issue is that, due to toroidal plasma shape, each constant pressure surface is shifted towards the Low Field Side (LFS) of tokamaks. This is known as Shafranov shift (d_0), and the complete solution can be found in references [10, 11, 12, 13].

For this work, it is important to know relations between geometrical coordinates: radial (r) and vertical (z) positions, in terms of normalized radial coordinate (ρ) and poloidal angle (θ), as shown in equations 1-4.

$$\begin{gathered} \mathrm{r}(\rho,\theta) = \mathrm{r}_0 + \mathrm{d}_0(1-\rho^2) + \mathrm{a}\rho\cos\theta \\ \mathrm{z}(\rho,\theta) = \mathrm{z}_0 + \mathrm{a}\rho\sin\theta \end{gathered} \tag{1-4}$$

where:

r_0, z_0 are coordinates of plasma column center – indeed, it is the center of the most external closed plasma surface;

d_0 is the Shafranov Shift – a radial axis displacement of the most internal surface due to toroidicity effect;

The toroidicity effect is responsible for adding $[\mathrm{d_0}(1-\rho^2)]$ term in $\mathrm{r}(\rho,\theta)$ expression, implying that an internal surface radial displacement is always bigger than external ones, as it is shown in Figure 1-9. Note that equations 1-4 are valid only inside the plasma column ($0 \leq \rho \leq 1$).

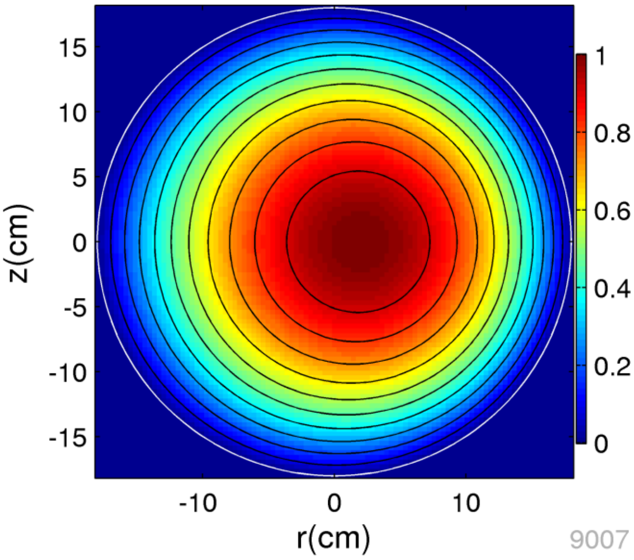

Figure 1-9: Normalized Pressure $p(r,z)$, for $\mathrm{d_0} = 2.0\ \mathrm{cm}$.

1.5. Plasma Radiation

1.5.1. Radiation Processes

The tokamak plasma is at a very high temperature. At these temperatures, plasma electrons and ions are emitting and absorbing electromagnetic radiation (photons) through some different physical processes.

The characterization of plasma properties is possible through the analysis of emitted radiation. The complete radiation processes can be very complicated since many different types of events can take place at same time [14, 15, 16, 17, 18, 19, 20]. Considering the three most important processes, we have:

a) Bremsstrahlung;

b) Recombination;
c) Line emission.

Bremsstrahlung is the emitted radiation by a slowing down electron when it is deflected by an ion. This process is called a free-free transition.

Recombination is a free electron capturing process by an ion. In this case, it is a free-bounded transition.

Line emission is the monochromatic radiation emitted by an already bounded electron that falls to a lower available energy level inside the atom. It is called a bounded-bounded transition.

1.5.2.Effective Z

In tokamak plasmas, it is expected that most of the available gas inside the tokamak chamber would be totally ionized. Considering that it is almost impossible to have just one kind of element in plasma, some different ion charges can be found. If just one element would be expected in plasma, all others are called impurities.

Therefore, in order to quantify emitted radiation, an effective charge Z is defined according to equation 1-5 [21].

$$Z_{eff} = {\sum n_i Z_i^2}/{\sum n_i Z_i} = \sum \frac{n_i Z_i^2}{n_e} \qquad \text{1-5}$$

where:

i is an index for each element type;
n_i is the respective element density (cm^{-3});
Z_i is the respective element charge (Z);
n_e is the electron density (cm^{-3}).

Z_{eff} works as a weighted mean of ions charges and densities.

1.5.3.Plasma Optical Emissivity

Plasma emissivity is usually calculated according to equation 1-6 [6, 22].

$$\frac{\varepsilon}{n_e n_z} = C_L Z_{eff}^3 T_e^{-3/2} + C_R Z_{eff}^2 T_e^{-1/2} + C_B Z_{eff} T_e^{1/2} \qquad \text{1-6}$$

where:

$\mathcal{E}$ is the emitting power density, or optical emissivity (W/cm^3);

T_e is the electron temperature $(°K)$;

n_e, n_z are electron and ion densities, respectively (cm^{-3});

C_L, C_R, C_B are constants for Line emission, Recombination and Bremsstrahlung processes, respectively. Each constant must be dimensionally correct according to equation terms.

According to equation 1-6, Optical Emissivity $(\mathcal{E})$ changes due to:

a) Radiation process;
b) Effective Z (or ions and impurities density);
c) Electron temperature;
d) Electron density;

Real emissivity from each radiation process is not measurable directly, although some assumptions can be done according to the diagnostic spectral characteristics. Moreover, the radial dependence of emissivity parameters, such as density, temperature and impurities concentration can be modeled from plasma emissivity equations [5, 6, 15, 23].

1.6. Optical Diagnostics

Optical diagnostics considered in this work measure electromagnetic radiation through a slit. For this purpose, semiconductor sensors (photodiodes array) with adequate spectral response were conveniently placed, allowing specific filters to be placed between sensors and plasma. Used diagnostics are:

a) Bolometer;

b) Soft X-Rays.

The bolometer diagnostic [24, 25] measures electromagnetic radiation in a wide spectrum range: it covers from near infrared $(\sim 1eV)$ up to low energy x-rays $(\sim 1keV)$. Basically, it measures all emitted radiation from the plasma. Description of the last hardware version for this diagnostic in TCABR is found in reference [25]. Figure 1-10 shows its geometric configuration.

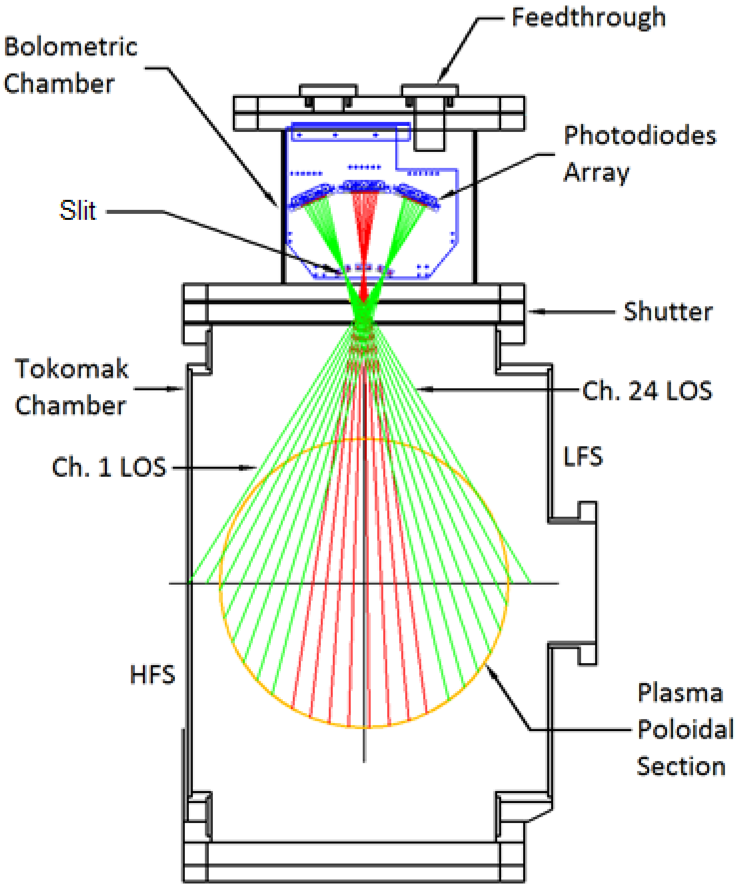

Figure 1-10: Bolometer Geometric Configuration[3]

The soft X-rays diagnostic [26, 27] measures electromagnetic radiation in a spectrum range starting at UV $(\sim 100eV)$ up to low energy x-rays $(\sim 1keV)$ due to a small beryllium filter conveniently chosen. Figure 1-11 shows its geometric configuration in TCABR.

---

[3] Source: Reference [25].

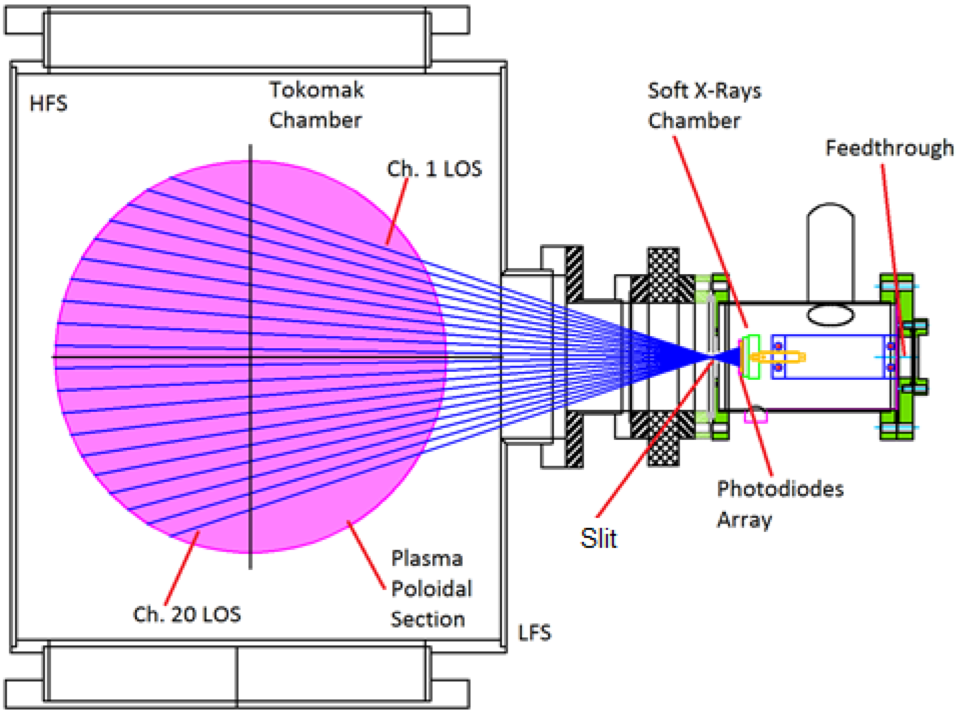

Figure 1-11: Soft X-Rays Geometric Configuration[4]

In this kind of geometry, each diagnostic sensor (photodiode) receives radiation from a variety of points with different emissivity, along a respective line-of-sight. Figure 1-12 shows an SXR example on how emissivity changes along each line-of-sight.

---

[4] Source: Reference [27].

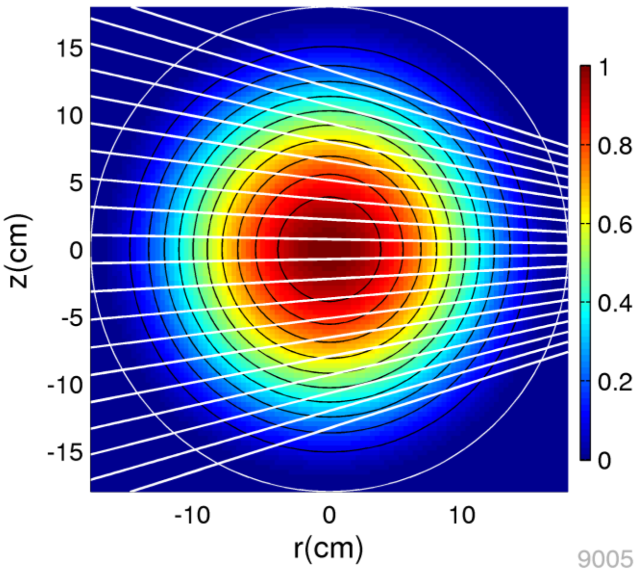

Figure 1-12: Normalized Plasma Emissivity Variation Along
Each SXR Channel/Sensor Line-of-Sight.

Therefore, the effective signal measured by each sensor is the resulting line integrals of the emitted radiation in the solid angle covered by the respective sensor [28], attenuated by the slit geometric characteristics, according to equation 1-7. This equation is known as Radon Transform [29], except by K_α term.

$$L_{ch} = K_\alpha . \int_{l_{ch}} E(\rho, \beta)\, dl \tag{1-7}$$

where:

a) L_{ch} (Volts) is the measured luminosity by each channel/sensor;

b) K_α $(dimessionless)$ is the slit signal attenuation for each channel due to radiation incidence angle;

c) l_{ch} (cm) is the line integration path corresponding to the respective channel line-of-sight;

d) $E(\rho, \beta)$ (Volts/cm) is the emissivity;

e) β is a set of free parameters related to the chosen plasma emissivity profile model that will be discussed in next chapters.

An effective emissivity reconstruction method was implemented to estimate plasma emission profiles from measured luminosity, without using conventional unfolding procedures, like Abel's inversion method. The Abel's inversion method was avoided here, because it produces strong fluctuations in the reconstructed method due to the use of numerical differences between experimental data to estimate the luminosity derivative [30].

1.7. Chapter Summary

This chapter briefly described the TCABR tokamak, necessary MHD equations, plasma pressure profiles, optical emissivity equation and optical diagnostics used for plasma experimental measurements: Bolometer and Soft X-Ray.

It also presented the main advantage and limitation of optical plasma diagnostics and introduced the Radon Transform that sets the relation between emissivity profile and measured luminosities. A more detailed mathematical approach on Radon Transform is done in next chapter.

2. Methodology

2.1. Tomography Methodology

Tomography [14, 28] is an unfolding method that makes possible to reconstruct object images from measured projections of a physical quantity. One important challenge concerning Tomographic methods is an adequate choice of measured projections, depending on the object geometry.

In this work, tokamak's plasma is the object of study, emitting radiation spontaneously in a wide spectrum range, including visible light. Thus, measured projections are the luminosity received through a slit in specific detectors arrangement.

2.2. Measured Luminosity

It is possible to calculate the total emitted power by a small plasma region according to equation 2-1:

$$P_{Emitted} = \int_V \mathcal{E}(\rho, \beta)\, dV \qquad \text{2-1}$$

where:

a) Optical emissivity $\mathcal{E}\ (W/cm^3)$ is an isotropic power flux from each plasma point;

b) $dV(cm^3)$ is a differential element of volume on the emitting plasma region.

Therefore, the total emitted power can be written in terms of the Solid Angle of the considered plasma region by:

$$P_{Emitted} = \int_V \mathcal{E}\, dV = \int_l \mathcal{E}S\, dl = \int_l \mathcal{E}\Omega d^2\, dl \qquad \text{2-2}$$

where:

c) Transversal Area $S\ (cm^2)$ that defines the element of volume dV

d) Solid Angle $\Omega\ (sr)$ that determines the Area S, considering the respective sphere center at slit;

e) Element of length $dl\ (cm)$ along a sensor line-of-sight;

f) Distance d between slit and plasma emitting point.

Calculating the emitted power that reaches the slit, remembering that the emitted power is supposed to be isotropic, we get equation 2-3.

$$P_{Fence} = P_{Emitted}\frac{S_F}{S_{sp}} = P_{Emitted}\ \frac{S_F}{4\pi.d^2} \qquad 2\text{-}3$$

where:

g) $S_F(cm^2)$ is the slit area;

h) $S_{sp}(cm^2)$ is the sphere area that is centered at plasma emitting point and its radius is the distance d to the slit.

Now, considering the total power that reaches each diagnostic sensor, we get equation 2-4.

$$P_{Sensor} = P_{Fence}K_C K_\alpha \qquad 2\text{-}4$$

where:

i) $K_\alpha\ (dimensionless)$ is the slit signal attenuation only due to light incidence angle. See Appendix B – Slits Optical Attenuation for calculations;

j) $K_C\ (dimensionless)$ is related to all other attenuation effects inside diagnostic chamber, but incidence angle.

The incident light power in a diagnostic sensor is converted to a current according to sensor optical response. Then, this current is amplified to a voltage before going to an ADC system. In ADC, signals are digitalized and finally stored in a database. This is represented in equation 2-5.

$$U = P_{Sensor}\eta G \qquad 2\text{-}5$$

where:

k) $U\ (V)$ is the measured signal by ADC system;
l) $\eta\ (A/W)$ is the sensor optical response;
m) $G\ (V/A)$ is the current-to-voltage amplifier gain.

Thus, replacing all equations, the result is given by equation 2-6.

$$U = K_\alpha \int_l \frac{1}{4\pi} \mathcal{E}(\rho,\beta) S_F \Omega K_C \eta G \, dl \qquad 2\text{-}6$$

Now, defining 'luminosity' (voltage), according to equation 2-7:

$$L_{Ch} = U \qquad 2\text{-}7$$

Additionally, defining the 'emissivity' (voltage per length), according to equation 2-8:

$$E(\rho,\beta) = \frac{1}{4\pi} S_F \Omega K_C \eta G . \mathcal{E}(\rho,\beta) \qquad 2\text{-}8$$

We can recover equation 1-7:

$$L_{ch} = K_\alpha . \int_{l_{ch}} E(\rho,\beta) \, dl \qquad 1\text{-}7$$

Note that the luminosity in a channel (L_{ch}) is defined to be the Radon Transform (RT) of emissivity (E) multiplied by respective channel slit attenuation (K_α), according to equation 1-7. In this work, luminosity, radiation and brightness will be used as synonyms once a wide spectrum range is covered by Bolometer and Soft X-Ray detectors.

A simplifying fact is that a surface defined by a fixed solid angle rises according to square distance from its spherical center and an isotropic electromagnetic radiation power falls according to square distance inverse from its spherical center. Thus, when these two conditions are considered in this problem, they cancel each other allowing measured signal to be calculated by just a line integral.

Since the sensor optical response is variable according to the radiation spectral band and this band is relatively wide, it is not possible to calculate the real emissivity in terms of the spectral band. Thereby, in this work, most of graphics will indicate 'arbitrary units' (a.u.) for luminosity (V) and for emissivity (V/cm).

These calculations show that it is possible to simulate luminosity intensity, channel-by-channel, and each result is taken as a tomography system projection.

2.3. Emissivity Profile Generalities

Since ohmic discharges are considered, we presume that plasma emissivity has its maximum at central position of the poloidal plane, decreasing monotonically from center to border, where $\rho = 1$. In fact, any function that fits this property could be used as an emissivity function. In this case, measured projections are higher in diagnostic central channels than in border ones.

Some common plasma emissivity functions that follow these properties are defined and discussed in Chapter 3. In the following sections, it is considered that the emissivity profile is described by a chosen plasma emissivity function that depends on some parameters ($\beta' s$), therefore, $E = E(\rho, \beta)$.

2.4. Code Implementation

Code was implemented using Matlab™. This implementation was divided in some specific codes:

a) Plasma Modeling Function;
b) Diagnostic Modeling Function;
c) Radon Transform Function;
d) Simulating Data Function;
e) Database Get Data Function;
f) Parameters Fitting Function.

Plasma Modeling Function sets all necessary plasma parameters according to the type of the profile chosen: horizontal position, vertical position, minor radius, Shafranov displacement and all emissivity profile parameters. Figure 2-1 shows Plasma Modeling Function output in a graphic mode. All these parameters, one-by-one, can be set to a fixed value or leave as fitting free parameter.

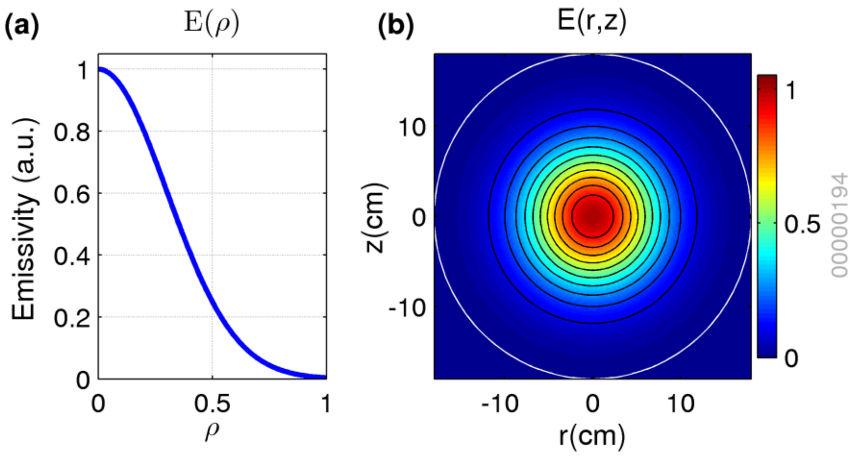

Figure 2-1: Plasma Modeling Function Output

(a) Emissivity as a function of ρ and (b) Emissivity as a function of x and z.

Diagnostic Modeling Function sets all necessary parameters related to detector type hardware: define line-of-sight equations, channel slit attenuation and active channels. Figure 2-2 shows Diagnostic Modeling Function output in a graphic mode. Active channels can also be chosen according to the experimental data available, once some diagnostic channels may not be working due to a hardware fault in some discharges.

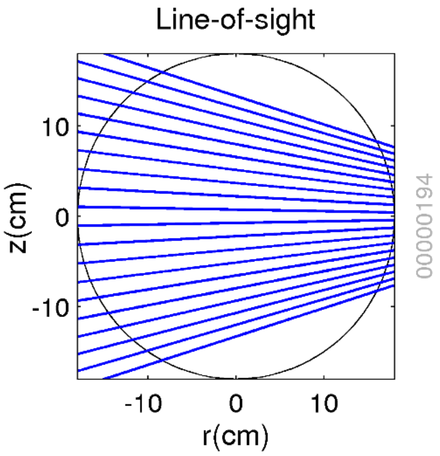

Figure 2-2: Diagnostic Modeling Function Output. Line-of-sight for SXR is shown.

Radon Transform Function uses plasma and diagnostic functions in order to calculate the Radon Transform, that is, the line integral of emissivity for each active channel. This function input and output data are shown in Figure 2-3.

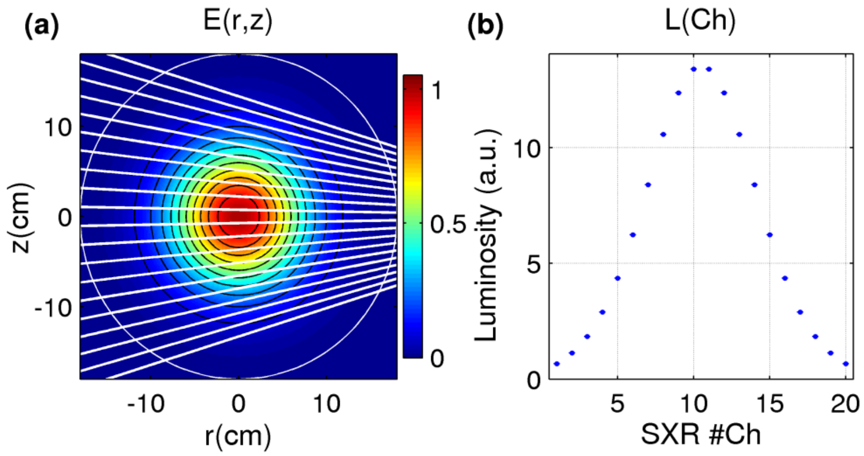

Figure 2-3 Radon Transform Function (a) Input and (b) Output

Simulating Data Function uses the last 3 functions to simulate luminosity and the related uncertainty can be set up in this code.

Database Get Data Function reads the real measured data by discharge number and chosen diagnostic. Estimated uncertainty and working time interval are set up at this time.

Parameters Fitting Function uses pre-programmed least square method to fit free parameters by receiving the plasma emissivity model, the detector model, the Radon Transform Function, the initial conditions and the input data in order to calculate fitting parameters. This function workflow is shown in Figure 2-4. Input data can be the simulated luminosity obtained from Simulating Data Function or the real measurements obtained from Database Get Data Function.

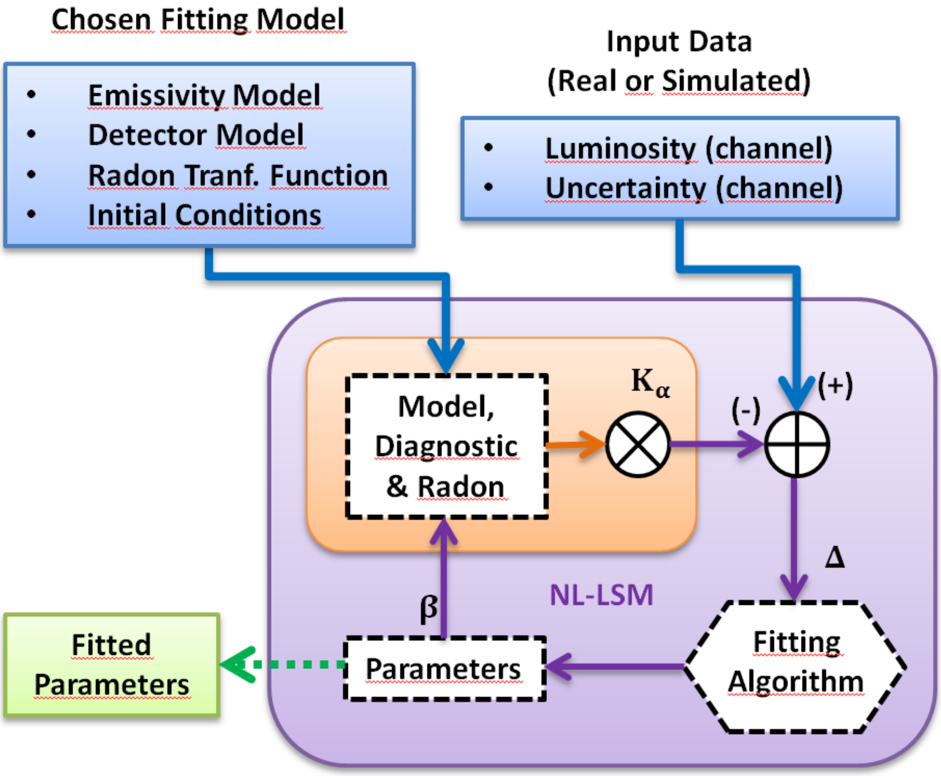

Figure 2-4: Parameters Fitting Function Workflow

Since Parameters Fitting Function is working with a non-linear system, the Least Square Method with Gauss-Marquardt approach, also known as Levenberg–Marquardt algorithm, is used [31]. This method is, basically, a Least Square Method that works interactively up to get free parameters properly fitted.

Once this method uses monotonic emissivity profiles and integration is done over the line-of-sight, it does not have the inconvenience of dealing with a numerical inversion like Abel’s method.

A numerical inversion can have some statistical difficulties inherent to the unfolding process of emissivity reconstruction. It may result in high uncertain due to some noise present at input signal [1, 2, 30, 32].

2.5. Chapter Summary

In this chapter, tomographic method is mentioned, the correspondence between optical emissivity ($\mathcal{E}$), emissivity (E) and luminosity (L) is described in a more detailed way and some emissivity profile generalities are mentioned.

This chapter also describes all parts of the implemented code and the Parameters Fitting Function Workflow. The next chapter will present the mathematical functions considered in this work to model plasma emissivity profile.

3. **Plasma Emissivity Profile Models**

In order to model the plasma emissivity it is considered that the equilibrium emissivity depends only on the magnetic surface. The position of these surfaces can be defined by a normalized coordinate ρ, that is zero at center and raises linearly up to 1 at plasma border.

In this work, three important emissivity profile models suitable to deal with the Equilibrium emissivity in ohmic discharges are considered:

a) Parabolic-in-Law;
b) Gaussian;
c) Bessel function.

These models are discussed, one by one, in following sections for the two optical diagnostics considered in this work: Soft X-Rays and Bolometer. Here, β is replaced by a set of parameters related to each profile model.

3.1. Parabolic-in-Law Profiles

Parabolic-in-law profiles are the most common used ones for plasma parameters modeling. As examples, parabolic-in-law profiles are used for modeling electron density, electron temperature and ionic temperature. This profile model is given by equation 3-1 below.

$$E(\rho) = E_0(1 - \rho^2)^{\gamma} \qquad \text{3-1}$$

Parabolic-in-law profile model has two free parameters: E_0 and γ. When fitting both parameters, it is possible to reproduce a wide variety of plasma emissivity profiles. Since E_0 is just a scale factor, it was set to the unit in the examples shown in this section. Also, for simplicity, parabolic-in-Law profiles will be referred, for simplicity, just as 'Parabolic'.

In Figure 3-1, parabolic emissivity profiles are shown for E_0 equal to 1.0 and several γ values ($\gamma =$ 0.2, 0.5, 1.0, 2.5 and 6.0). In this kind of profiles, if γ is close to the unit, profile is more likely a parabola – as expected. However, when considering higher γ values, the profiles become more peaked for low ρ and the function tail gets closer to an exponential, decreasing to zero very fast. On the contrary, for low values of γ, the profiles become closer to an uniform profile for low ρ and falls abruptly to zero when ρ is close to the unit.

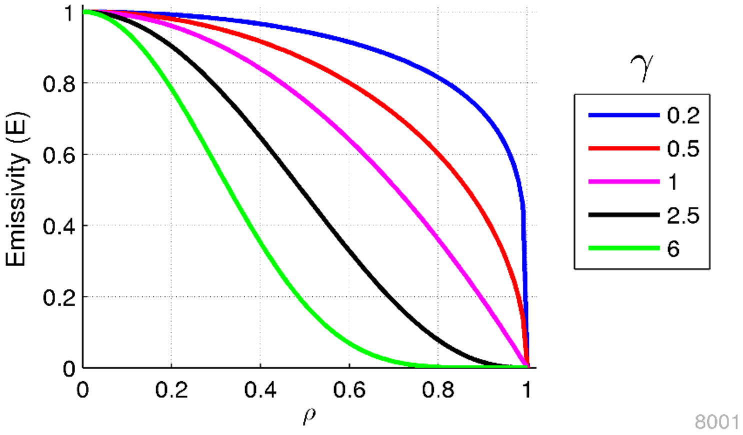

Figure 3-1: Parabolic Emissivity Profiles

In order to illustrate the relationship between the parabolic profile and the typical shape of the correspondent luminosity measured in Bolometer and Soft X-Ray diagnostics, some examples are shown in next sections.

3.1.1.Parabolic Profiles at Bolometer Diagnostic

For bolometer diagnostic case, Figure 3-2 and Figure 3-3 show expected results for simulated parabolic profiles and calculated luminosity, where γ has been set for 2 different values: 0.5 and 1.0, respectively. Here, it is possible to understand that as γ increases, emissivity becomes weaker at plasma border (higher ρ) and luminosity become more peaked.

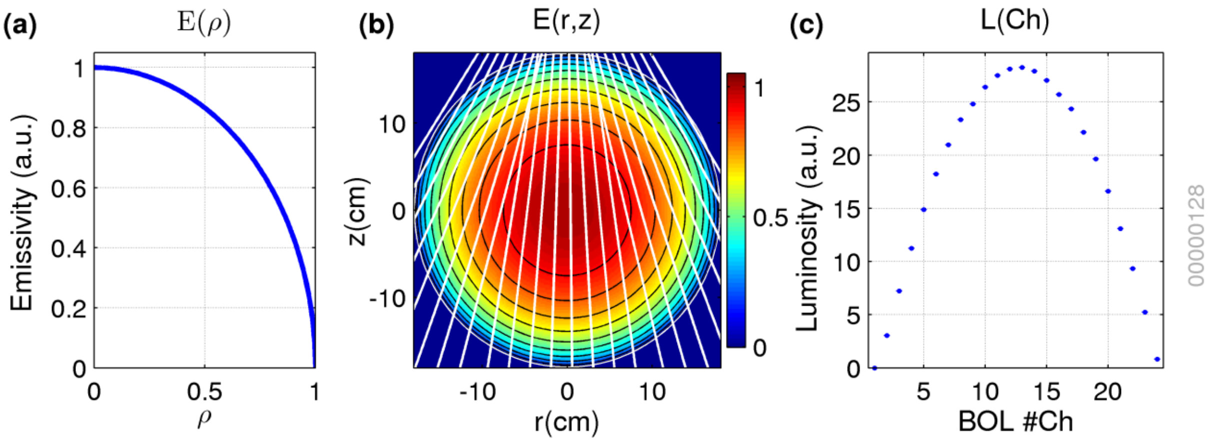

Figure 3-2: Bolometer Simulated Parabolic Profile, E_0=1.0, γ=0.5,

(a) E(ρ), (b) E(r,z), (c) L(Ch).

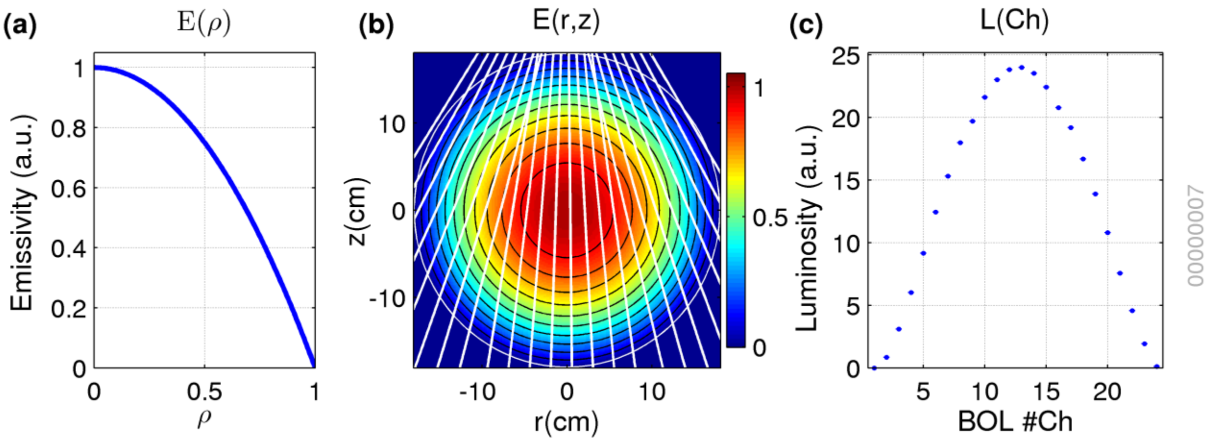

Figure 3-3: Bolometer Simulated Parabolic Profile, E_0=1.0, γ=1.0,

(a) E(ρ), (b) E(r,z), (c) L(Ch).

3.1.2. Parabolic Profile at Soft X-Rays Diagnostic

In Soft X-Rays case, Figure 3-4 and Figure 3-5 show expected values for parabolic simulated profiles and calculated luminosity, where γ has been set for 2 different values: 2.0 and 5.0, respectively. Since all Soft X-Rays channels line-of-sights are different from Bolometer, calculated luminosity plots have different shapes.

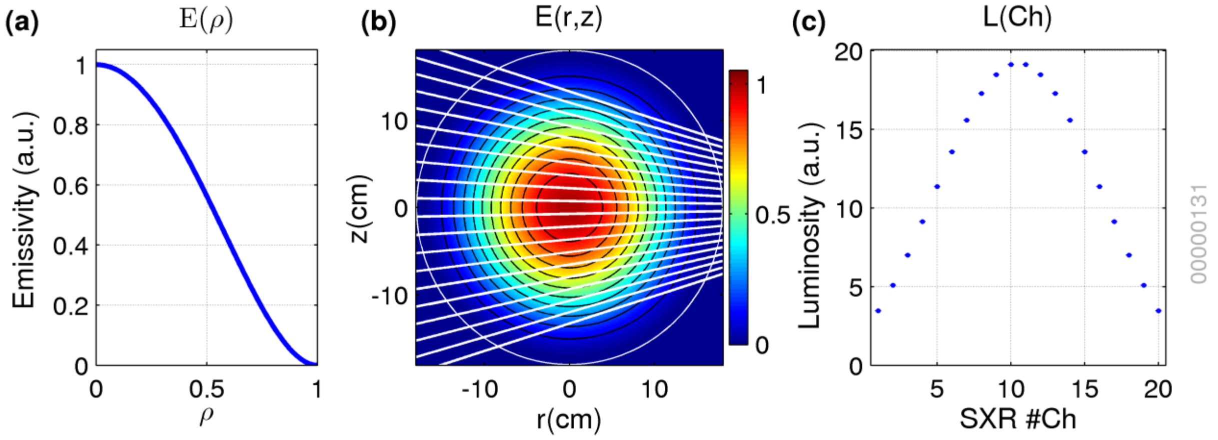

Figure 3-4: Soft X-Rays Simulated Parabolic Profile, E_0=1.0, γ=2.0,

(a) E(ρ), (b) E(r,z), (c) L(Ch).

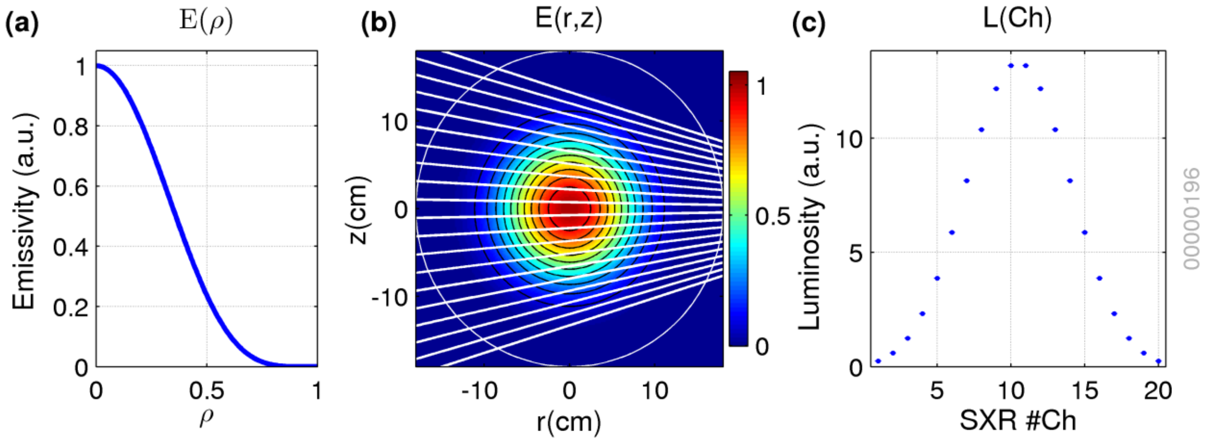

Figure 3-5: Soft X-Rays Simulated Parabolic Profile, E_0=1.0, γ=5.0,

(a) E(ρ), (b) E(r,z), (c) L(Ch).

3.2. Gaussian Profiles

The Gaussian function has a wide application in physics. As a model to the Equilibrium emissivity profile, the Gaussian function with low σ ($\lesssim 0.3$) has some interesting properties like:

1. Amplitude goes to zero as ρ get closer to unit (plasma border);
2. Gaussian parameter σ returns the width of this function.

An emissivity profile model according to equation 3-2 is known as Gaussian plasma emissivity profile.

$$E(\rho) = E_0 e^{-\frac{1}{2}\left(\frac{\rho}{\sigma}\right)^2} \qquad 3\text{-}2$$

Gaussian emissivity profile model has two free parameters: E_0 and σ. In Figure 3-6, Gaussian emissivity profiles are shown for E_0 equal to 1.0 and several σ values ($\sigma =$ 0.1, 0.18, 0.25, 0.4 and 0.6). In this kind of profiles, σ is a parameter related to the function width. When sigma reduces, Gaussian becomes narrower. On the contrary, as σ becomes big, Gaussian becomes wider.

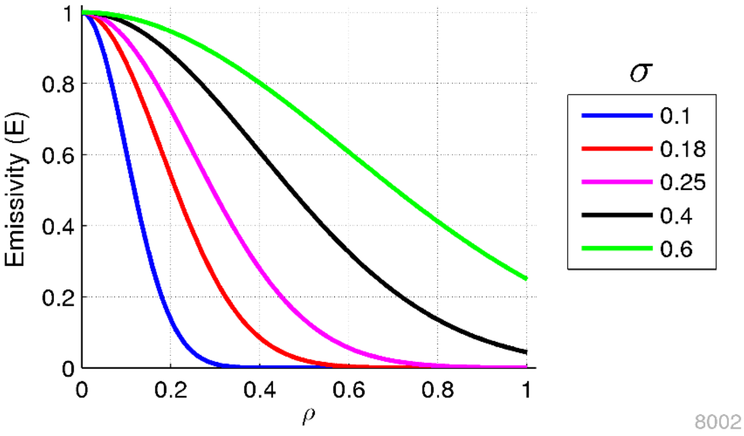

Figure 3-6: Gaussian Emissivity Profiles

Such profiles have a limitation in describing real emissivities when σ is not small enough ($\sigma \lesssim 0.3$). This happens due to emissivity does not converge to zero in the plasma border, giving a non-physical boundary condition.

Eventually, it may be more interesting to use Gaussian profiles instead of parabolic ones when parabolic model returns a high γ ($\gtrsim 5$), once the gaussian function has the profile width as a parameter. At the following examples of this section, E_0 was set to the unit, since it is just a scale factor.

3.2.1.Gaussian Profiles at Bolometer Diagnostic

For Bolometer diagnostic, Figure 3-7 shows expected values with a Gaussian simulated profile and calculated luminosity where σ has been set to 0.30. Notice that this case is not a realistic one because the emissivity drops too fast as ρ increases, as will be shown in next chapters. However, we choose this σ because a higher one would make emissivity profile does not converge to zero at plasma border.

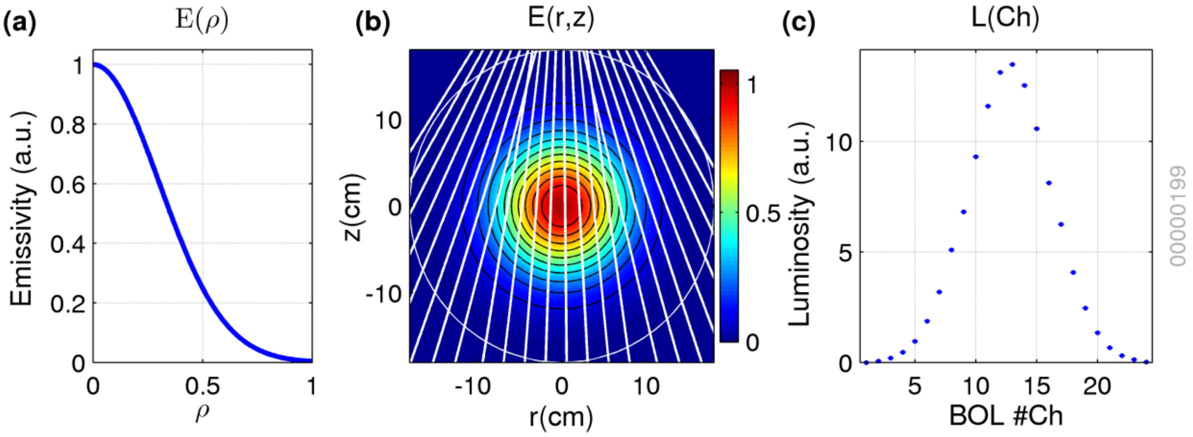

Figure 3-7: Bolometer Simulated Gaussian Profile, E_0=1.0, σ=0.30,

(a) E(ρ), (b) E(r,z), (c) L(Ch).

3.2.2.Gaussian Profile at Soft X-Rays Diagnostic

For Soft X-Rays diagnostic, Figure 3-8 shows expected values for simulated Gaussian profiles and calculated luminosity, where σ has been set to 0.20. This parameter value is closer to the experimental σ value observed in TCABR, as it is shown in section 5.1.1.3.

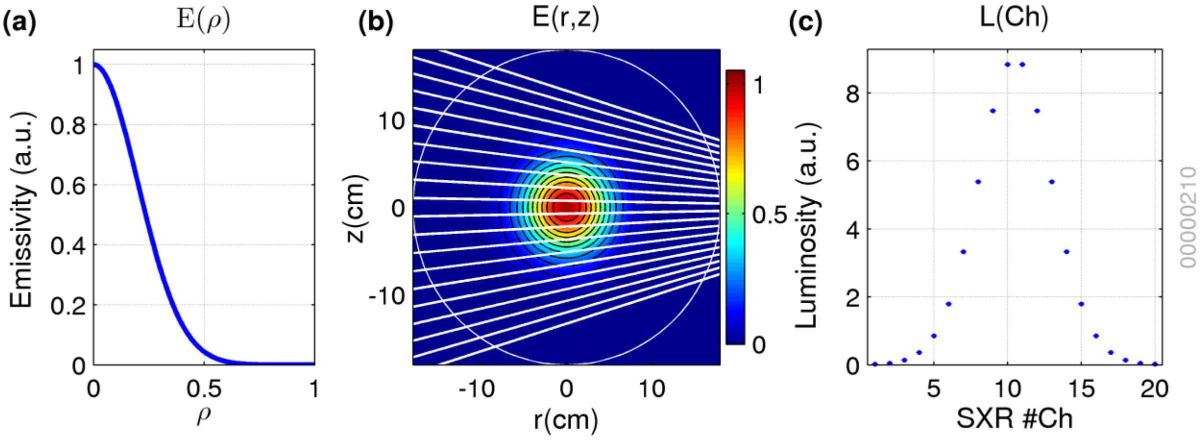

Figure 3-8: Soft X-Rays Simulated Gaussian Profile, E_0=1.0, σ=0.20,

(a) E(ρ), (b) E(r,z), (c) L(Ch).

3.3. Bessel Based Profiles

Bessel functions are natural solutions to differential equations in cylindrical electromagnetic systems. Since a cylindrical coordinate system can approximate a toroidal one when a small toroidal displacement $\Delta\varphi$ is considered, Bessel function would work as a solution for emissivity profile modeling. These profile types have already been used in another tokamak, according to references [33, 34, 35, 36].

Defining six functions $J_R(\rho)$ based on Bessel Function of the First Kind $J_0(x)$, according to:

$$J_R(\rho) = J_0(\rho.x_R) \qquad 3\text{-}3$$

where x_R is the R^{th} root of Bessel $J_0(x)$, for $1 \leq R \leq 6$.

Table 3-1 shows all x_R values used by equation 3-3. Figure 3-9 shows all defined functions according to equation 3-3.

R	x_R
1	~ 2.4048
2	~ 5.5201
3	~ 8.6537
4	~ 11.7915
5	~ 14.9309
6	~ 18.0711

Table 3-1: Six first roots of Bessel function $J_0(x)$

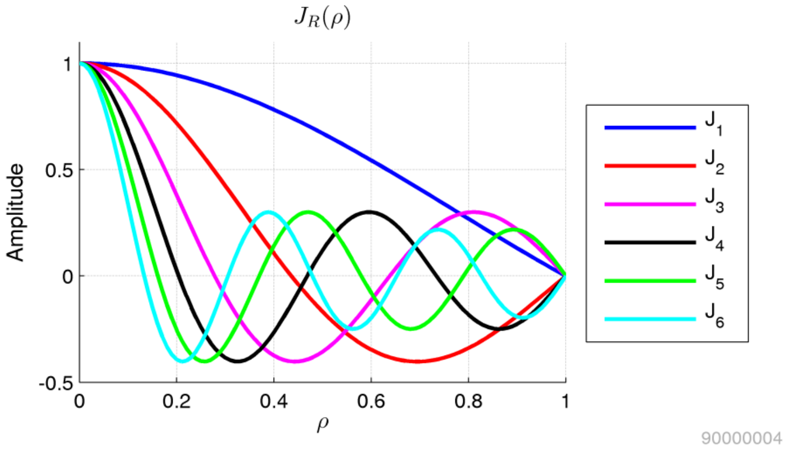

Figure 3-9: $J_R(\rho)$ functions

All six $J_R(\rho)$ functions are used to define the base for plasma emissivity profiles, according to 3-4:

$$E(\rho) = \sum\nolimits_R E_R . J_R(\rho) \qquad 3\text{-}4$$

In this work, a simplified reference to equation 3-4 will be described as "R Root(s) Bessel Emissivity Profile". Moreover, Bessel emissivity profile can have up to six free parameters E_R.

In Figure 3-10, Bessel emissivity profiles are shown using indicated E_R values in the caption.

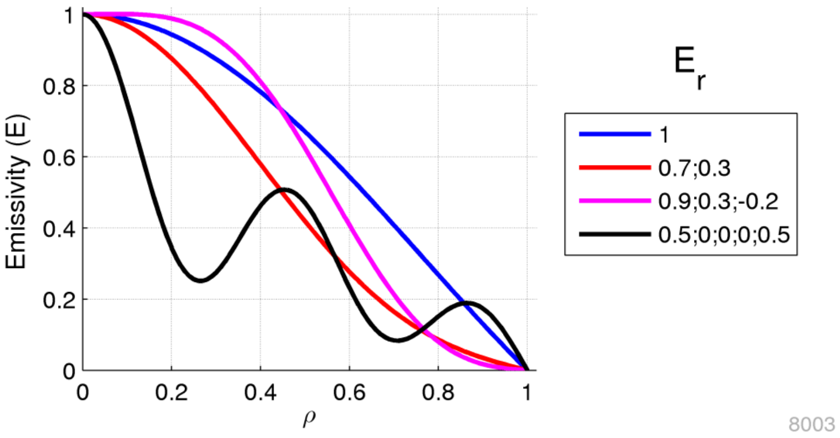

Figure 3-10: Bessel Emissivity Profiles

Such profiles may have problems if E_R values are not set properly. As it is shown in Figure 3-10, $E(\rho)$ could be non-monotonic. In other case, it could be negative without a physic meaning. Some examples of Bessel profiles are shown in the following sections.

3.3.1.Bessel Profiles at Bolometer Diagnostic

Figure 3-11 shows a three roots Bessel emissivity profile E_R=[0.9; 0.3; -0.2] for the Bolometer diagnostic case, as an example. When comparing this profile with the parabolic profile shown in Figure 3-2, it is possible to see that this one drops slower for small ρ, but falls more abruptly for Intermediaries ρ finishing in a smooth way when ρ goes to the unit, that is, at plasma border.

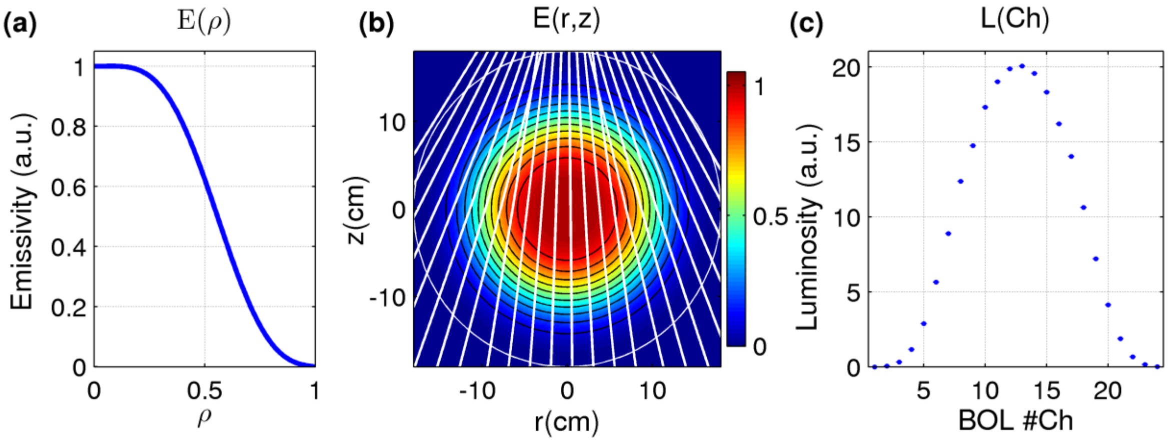

Figure 3-11: Bolometer Simulated Bessel Profile, E_R=[0.9; 0.3; -0.2],

(a) E(ρ), (b) E(r,z), (c) L(Ch).

3.3.2.Bessel Profiles at Soft X-Rays Diagnostic

For Soft X-Rays diagnostic, Figure 3-12 shows an example case for two roots Bessel emissivity profile E_R = [0.6; 0.4]. This emissivity profile shape is similar to the parabolic one shown in Figure 3-5.

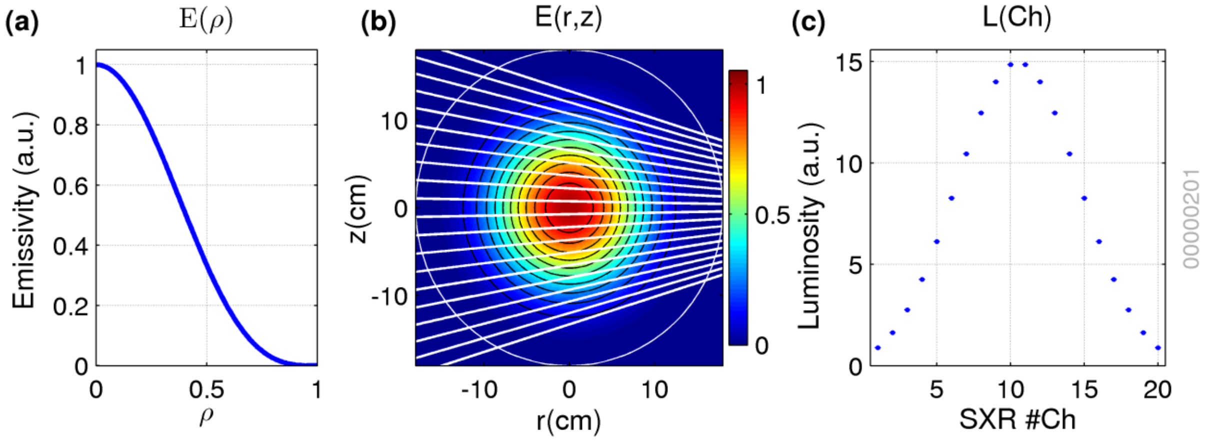

Figure 3-12: Soft X-Rays Simulated Bessel Profile, E_R=[0.6; 0.4],

(a) E(ρ), (b) E(r,z), (c) L(Ch).

3.4. Chapter Summary

In this chapter, three types of emissivity profile were defined: Parabolic, Gaussian and Bessel. The examples show how the luminosity profiles are related to the emissivity profiles for Bolometer and Soft X-rays cases.

The next chapter shows examples of how to detect errors in fitting conditions by comparing experimental and fitted luminosity shapes.

4. Numerical Simulations

In this chapter, simulated luminosity data, generated from a known emissivity profile, are fitted using implemented code in order to evaluate the effectiveness of the reconstruction method.

Some cases where simulated and fitted profiles are of the same kind will be omitted since they are considered trivial cases. Utilized emissivity model will be chosen, mainly, according to parameter returned from fitting process: parabolic profiles with high γ would be replaced by Gaussian ones and Gaussian profiles with high σ would be replaced by parabolic ones. Bessel will be used only to fit real data due to its interpretation dependents on real situations. Corrections in plasma position errors will be shown in next sections.

Simulating data free parameters can be:

a) Plasma emissivity profile parameters related to a chosen profile type;
b) Plasma geometric parameters: r_0 (radial plasma central position), z_0 (vertical plasma central position), a (plasma minor radius) and d_0 (Shafranov displacement);
c) Set of used diagnostic channels;
d) Slit attenuation effect (K_α), defined in section 1.6, can be removed when fitting simulated data.

This method allows each emissivity profile parameter and each geometric parameter to be fitted or to be fixed, one by one, according to convenience.

In this chapter, it must be considered:

a) If any plasma geometric parameter is neglected, it means that it is set to its respective default value ($r_0 = 0, z_0 = 0, a = 18.0, d_0 = 0$);
b) If diagnostic channel list is omitted, it means that all channels were considered for fitting ($Ch_{BOL} = 1\ to\ 24,\ \ Ch_{SXR} = 1\ to\ 20$);
c) Slit attenuation is turned off ($K_\alpha = 1, \forall\alpha$) in simulated and fitted data since no experimental data is used.

Many parameters were tested in order to cover experimental data and to check profile model limits and only important cases will be shown here.

In real cases, it will not be possible to compare experimental and fitted emissivities since only luminosity is accessible experimentally. So, conclusions must be based on the comparison between the experimental and fitted luminosity shapes once the emissivity profile is the result that we need to find.

In this chapter, figures have a specific format. They are divided into 5 plots: (a) Emissivity as a function of ρ (simulated and fitted data), (b) Fit residuals emissivity as a function of ρ, (c) Fit residuals emissivity as a function of r and z with diagnostic line-of-sight channels represented, (d) Luminosity for active channels (simulated and fitted data) and (e) Luminosity residuals for active channels.

4.1. Fitting Similar Profiles Types

In order to show the reconstruction method effectiveness, some fitting procedures were done using the same kind of profile type for both simulated data and the fitting function.

4.1.1.Bolometer

It was simulated a parabolic profile with parameters $\mathrm{E}_0 = 1.0,\ \gamma = 0.5$. The fitting model used was a parabolic profile (E_0, γ) and obtained results were $\mathrm{E}_0 = 0.9997$, $\gamma = 0.4997$. This fitting result is shown in Figure 4-1. Comparing both luminosities in plot (d) and their difference in plot (e), we found that there is no difference indicating that simulated data were fitted properly. Since it is a simulated case, we can check both emissivities in plots (a), (b) and (c), too.

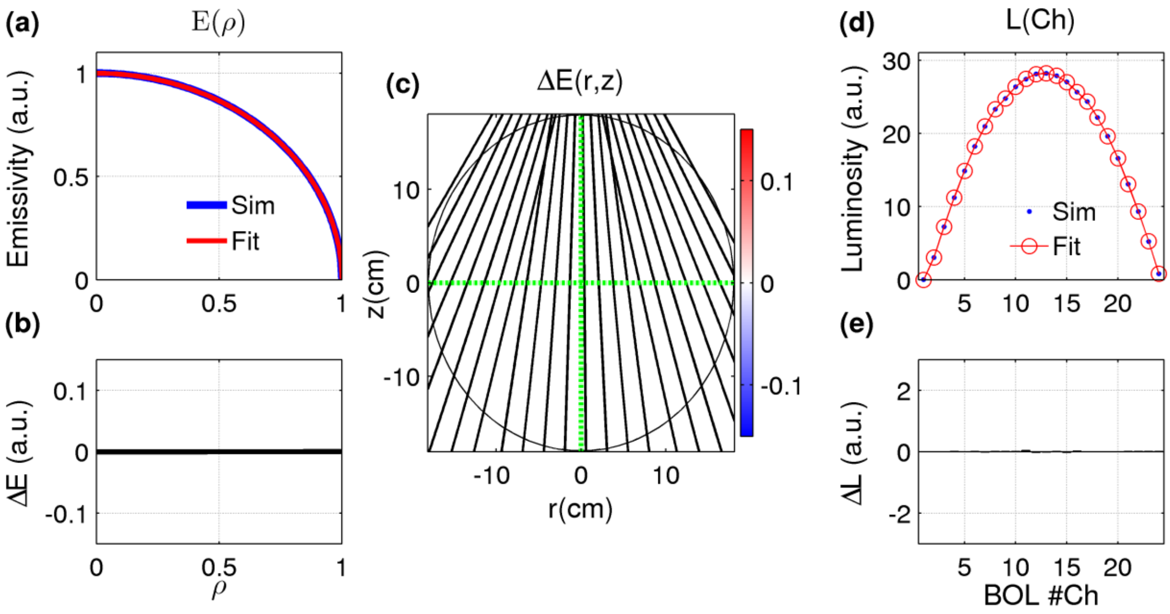

Figure 4-1: Bolometer Simulated Parabolic Profile, E_0=1.0, γ=0.5, Fitted by a Parabolic Profile. a) E(ρ), b) ΔE(ρ), c) ΔE(r,z), d) L(Ch), e) ΔL(Ch).

4.1.2.Soft X-Ray

Similarly, it was simulated a Gaussian profile with $\mathrm{E}_0 = 1.0,\ \sigma = 0.25$. The fitting model used was a Gaussian profile (E_0, σ) and obtained results were $\mathrm{E}_0 = 0.9974,\ \gamma = 0.2503$. This fitting result is shown in Figure 4-2. Like previous case, comparing both luminosities in plot (d) and their difference in plot (e), we found that resulting solution is, basically, equal to the simulated one. As in the previous Bolometer case, the simulated data were fitted properly.

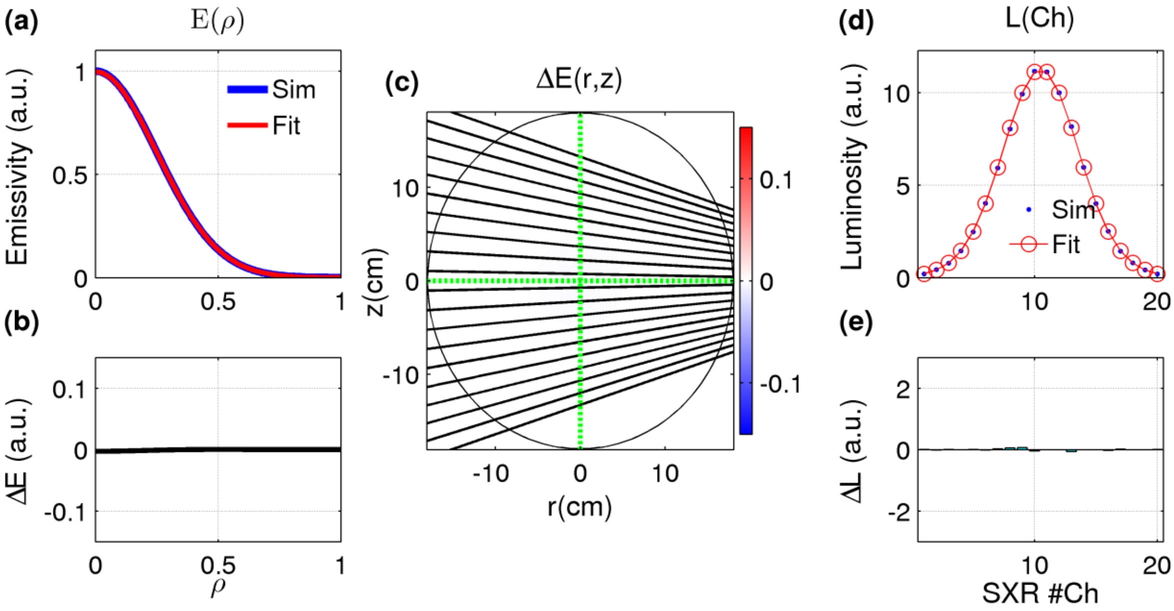

Figure 4-2: SXR Simulated Gaussian Profile, E_0=1.0, σ=0.25, Fitted by a Gaussian Profile. a) E(ρ), b) ΔE(ρ), c) ΔE(r,z), d) L(Ch), e) ΔL(Ch).

4.2. Plasma Radial Position Displacement

In this section, a displacement in plasma radial position was included in order to verify how implemented method deals with this condition. It is expected that the Bolometer would be more sensible than Soft X-Ray to plasma radial displacements due to its channels have almost vertical lines-of-sight, so a radial displacement in plasma or, equivalently, in the diagnostic hardware, would change the Bolometer channel that measures the maximum luminosity. This will be illustrated by the three simulations shown in this section.

The first simulated case is a parabolic profile with a moderate radial displacement ($\mathrm{E_0} = 1.0,\ \gamma = 1.0,\ \mathrm{r_0} = 1.0\ \mathrm{cm}$). The fitting model used was a parabolic profile $(\mathrm{E_0}, \gamma)$ and $\mathrm{r_0}$ has been intentionally neglected in order to evaluate the corresponding results. The resulting parameters were $\mathrm{E_0} = 1.12,\ \gamma = 1.30$ – this is a 12% error in core emissivity and 30% for gamma.

This fitting result is shown in Figure 4-3. Comparing both luminosities in plot (d) and their difference in plot (e), we found that ΔL shape is positive up to an intermediate channel then become negative up to last channel. So, such kind of ΔL would indicate a radial displacement in central plasma position that was not considered in fitting process. In fact, looking at plots (a), (b) and (c), we can realize that these results are inadequate.

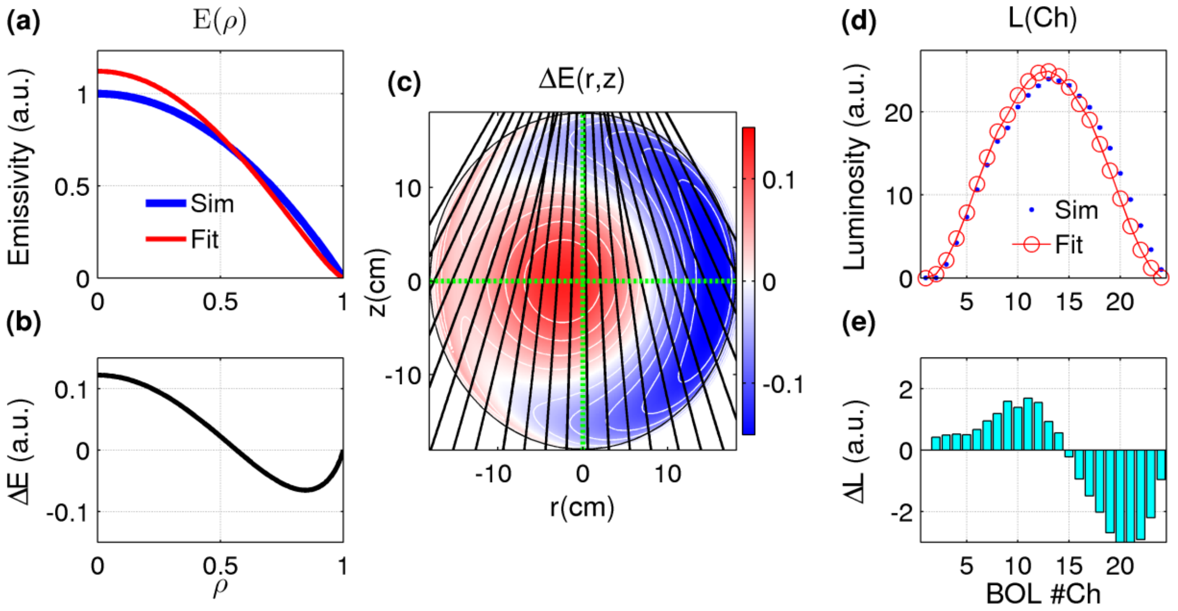

Figure 4-3: Bolometer Simulated Parabolic Profile, E_0=1.0, γ=1.0, r_0=1.0cm

Fitted by a Parabolic Profile (fixed r_0=0.0 cm). a) E(ρ), b) ΔE(ρ), c) ΔE(r,z), d) L(Ch), e) ΔL(Ch).

In the second simulation, we will let the radial position to be a free fitting parameter in order to correct the discrepancy seen in the previous case. It was simulated the same parabolic profile $(\mathrm{E_0} = 1.0,\ \gamma = 1.0,\ \mathrm{r_0} = 1.0\ \mathrm{cm})$ and the fitting model used was a parabolic profile with free radial displacement $(\mathrm{E_0}, \gamma, \mathrm{r_0})$. The fitted parameters are $\mathrm{E_0} = 1.0003,\ \gamma = 1.004,\ \mathrm{r_0} = 1.001\ \mathrm{cm}$, which recover the simulated profile with very low differences.

This fitting result is shown in Figure 4-4. Now, comparing both luminosities in plot (d) and their difference in plot (e), we found that ΔL is negligible, much lower than the previous case. This is an indication that this fitting procedure could restore the simulated data properly. In fact, looking at plots (a), (b) and (c), we cannot see any significant difference.

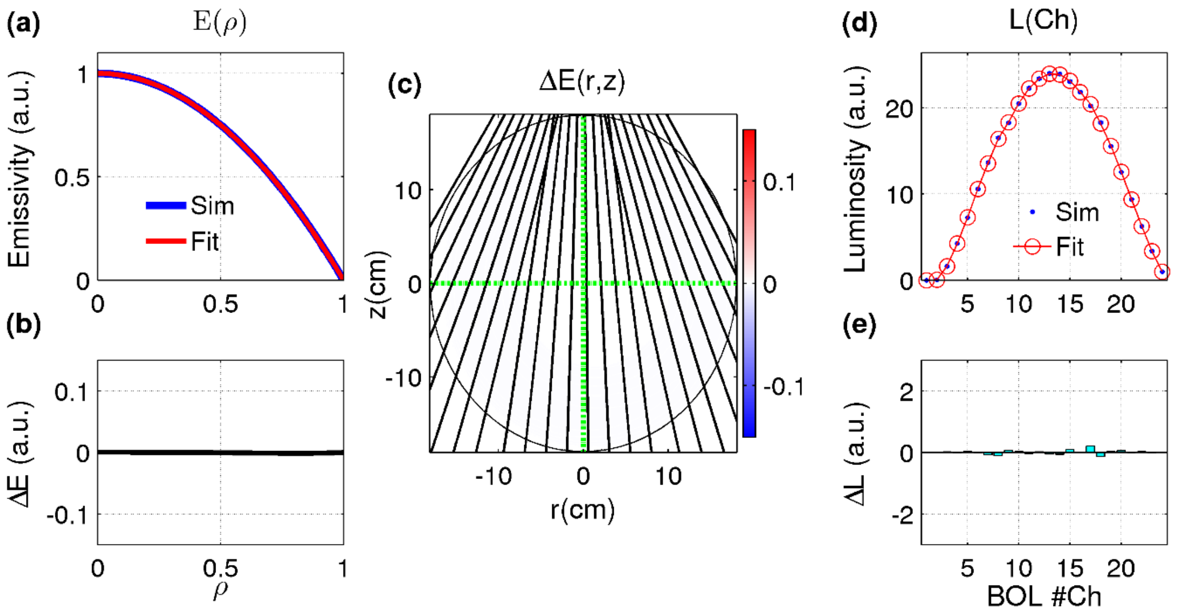

Figure 4-4: Bolometer Simulated Parabolic Profile, E_0=1.0, γ=1.0, r_0=1.0cm

Fitted by a Parabolic Profile (free r_0). a) E(ρ), b) ΔE(ρ), c) ΔE(r,z), d) L(Ch), e) ΔL(Ch).

In the third simulation, we will check what happens when fitting the plasma profile with the same radial displacement by the Soft X-Rays diagnostic. It was simulated a Gaussian profile with the same radial displacement ($\mathrm{E_0} = 1.0,\ \sigma = 0.25,\ \mathrm{r_0} = 1.0\ \mathrm{cm}$) and the fitting model was a Gaussian profile ($\mathrm{E_0}$, σ), and $\mathrm{r_0}$ has been intentionally neglected. The resulting parameters were $\mathrm{E_0} = 0.982,\ \sigma = 0.256$ – corresponding to small errors of 1.8% in the core emissivity and 2.4% in sigma.

This fitting result is shown in Figure 4-5. Comparing both luminosities in plot (d) and their difference in plot (e), we found that ΔL is negligible and we could conclude that this fitting result is adequate. However, when we look at plot (c), we are able to identify the difference between maximum emissivities positions – remember that emissivity in not accessible when experimental data is used.

Thereby, this example is a warning case since Soft X-Rays diagnostic may not indicate the presence of radial displacements. Indeed, the Bolometer diagnostic is much better than Soft X-Rays to detect radial displacements.

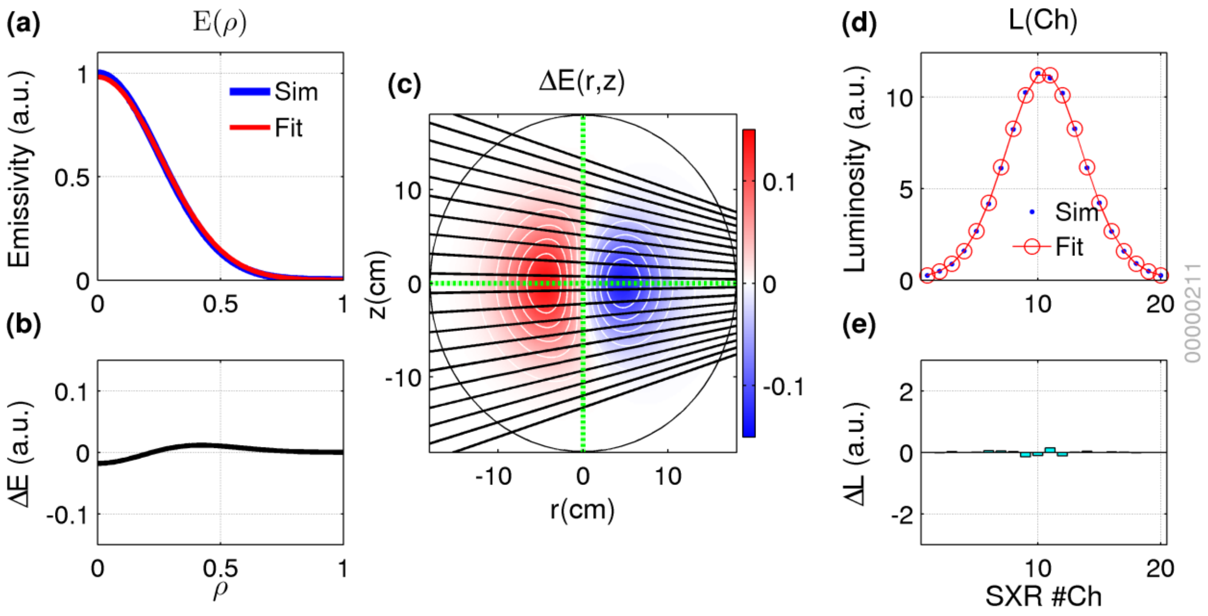

Figure 4-5: Soft X-Rays Simulated Gaussian Profile, E_0=1.0, σ=0.25, r_0=1.0 cm Fitted by a Gaussian Profile (fixed r_0=0.0 cm). a) E(ρ), b) ΔE(ρ), c) ΔE(r,z), d) L(Ch), e) ΔL(Ch).

4.3. Plasma Vertical Position Displacement

Similarly, a displacement in plasma vertical position was included in order to verify how implemented method works. Now, it is expected that the most sensible diagnostics to detect plasma vertical displacements would be the Soft X-Ray diagnostic due to its central channels have almost horizontal lines-of-sight. A vertical displacement in plasma or, equivalently, in diagnostic hardware, would change the Soft X-Ray channel that measures maximum luminosity. Three simulations are described in this section, too.

In the first case, it was simulated a Gaussian profile with a moderate vertical displacement $\mathrm{E_0} = 1.0,\ \sigma = 0.25, \mathrm{z_0} = 1.0\ \mathrm{cm}$. The fitting model used was a Gaussian profile $(\mathrm{E_0}, \sigma)$ in which $\mathrm{z_0}$ has been intentionally neglected. The resulting parameters were $\mathrm{E_0} = 0.963,\ \sigma = 0.245$ – corresponding to a 3.7% error in the core emissivity and 2% in sigma.

This fitting result is shown in Figure 4-6. Comparing both luminosities in plot (d) and their difference in plot (e), we found that ΔL shape is positive up to an intermediate channel then become negative up to last channel. Again, such kind of ΔL would indicate a vertical displacement in central plasma position that was not considered in fitting process.

This is a similar case to the first one shown in previous section. However, when looking only at plots (a) and (b) we could not realize that this fit is not so good.

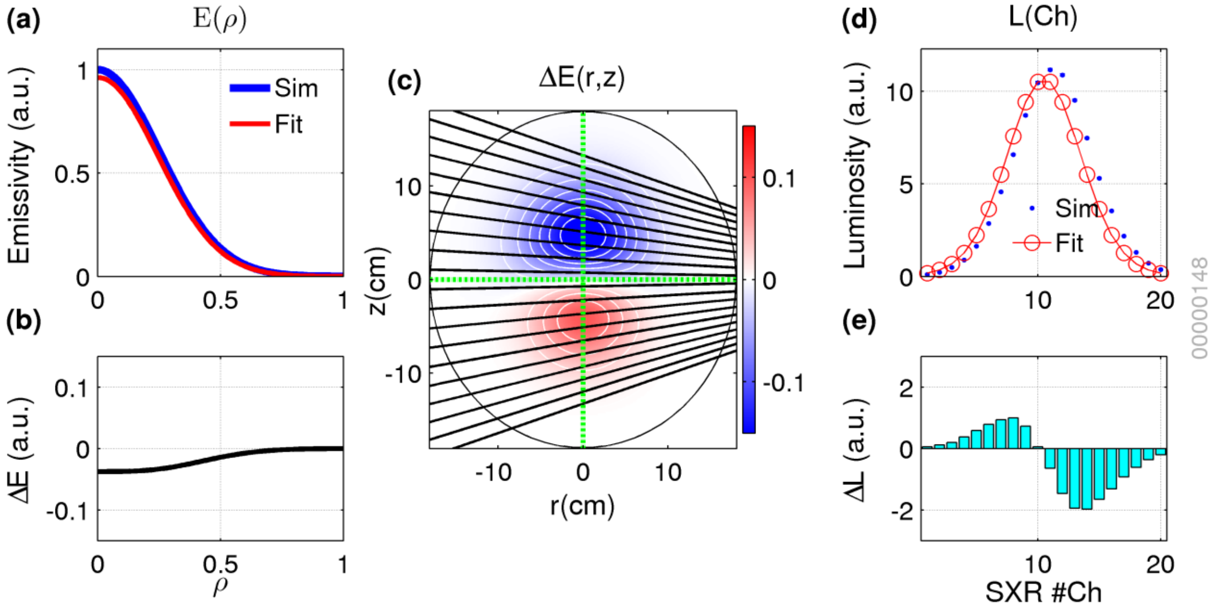

Figure 4-6: Soft X-Rays Simulated Gaussian Profile, E_0=1.0, γ=0.25, z_0=1.0cm Fitted by a Gaussian Profile (fixed z_0=0.0 cm). a) E(ρ), b) ΔE(ρ), c) ΔE(r,z), d) L(Ch), e) ΔL(Ch).

In the second simulation, we will try to correct this discrepancy. It was simulated the same Gaussian profile $(\mathrm{E}_0 = 1.0,\ \sigma = 0.25, \mathrm{z}_0 = 1.0\ \mathrm{cm})$ and the fitting model used was a Gaussian profile with free vertical displacement $(\mathrm{E}_0, \sigma, \mathrm{z}_0)$. The obtained results are $\mathrm{E}_0 = 1.000, \sigma = 0.250, \mathrm{z}_0 = 0.998\ \mathrm{cm}$, which recover the simulated profile with very low differences.

This fitting result is shown in Figure 4-7. Now, comparing both luminosities in plot (d) and their difference in plot (e), we found that ΔL is negligible. This is an indication that the fitting procedure could restore simulated data properly. The resulting emissivity is shown in plots (a), (b) and (c), confirming what was seen in the luminosity.

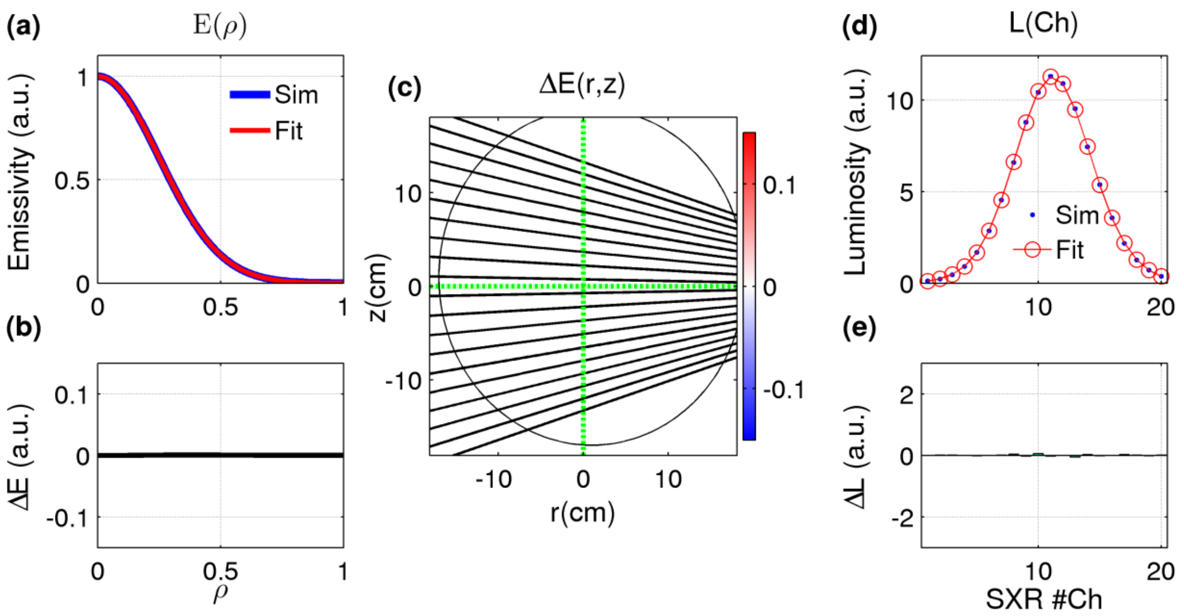

Figure 4-7: Soft X-Rays Simulated Gaussian Profile, E_0=1.0, σ=0.25, z_0=1.0cm Fitted by a Gaussian Profile (free z_0). a) E(ρ), b) ΔE(ρ), c) ΔE(r,z), d) L(Ch), e) ΔL(Ch).

In the third simulation, we will check what happens when Bolometer diagnostic is used. It was simulated a parabolic profile with the same vertical displacement ($\mathrm{E_0} = 1.0$, $\gamma = 1.0$, $\mathrm{z_0} = 1.0\ \mathrm{cm}$). The fitting model used was a parabolic profile $(\mathrm{E_0}, \gamma)$ and $\mathrm{z_0}$ has been intentionally neglected. The resulting parameters were $\mathrm{E_0} = 0.908$, $\gamma = 0.774$ – this is a 9.2% error in E_0 and 23% in γ.

This fitting result is shown in Figure 4-8. Comparing luminosities in plot (d), no significant difference can be observed. If data in plots (d) and (e) are used to calculate $\Delta L/L$, the maximum relative error is less than 3% in most channels. Thus, we could conclude, wrongly, that this result would be satisfactory.

This case shows that when using the bolometer diagnostic, it is very important to know previously the vertical position of the plasma, since an error in the vertical position may not be detected from the comparison between the experimental data and the fitted luminosities. In addition, the fitted parameters may be very different from the real ones.

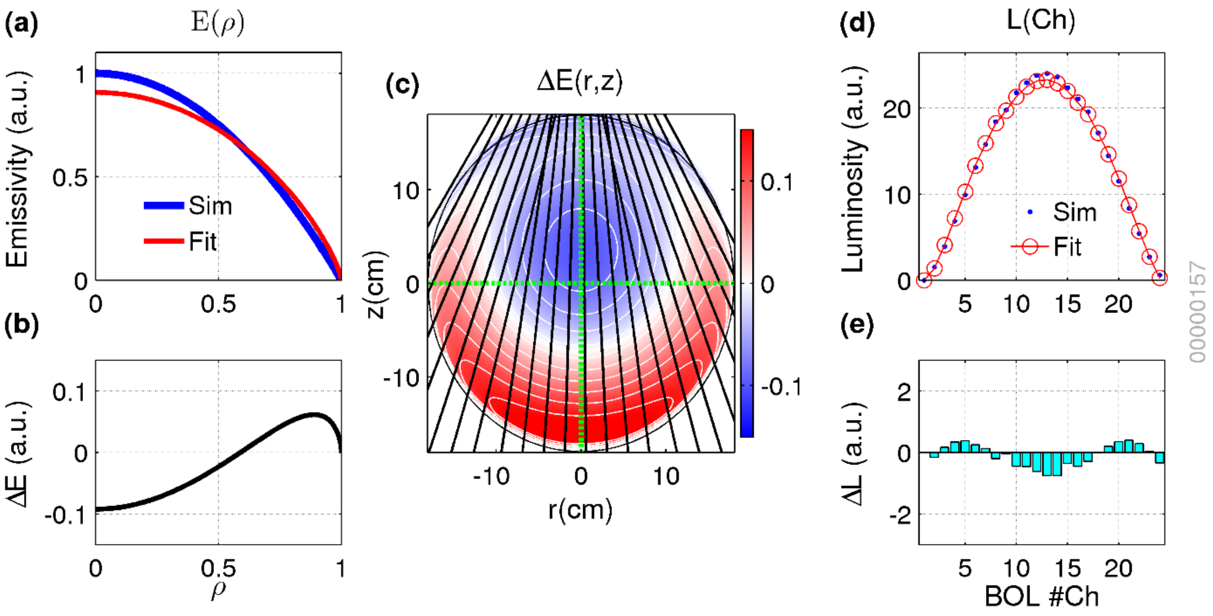

Figure 4-8: Bolometer Simulated parabolic Profile, E_0=1.0, γ=1.0, z_0=1.0cm Fitted by a parabolic Profile (fixed z_0=0.0 cm). a) E(ρ), b) ΔE(ρ), c) ΔE(r,z), d) L(Ch), e) ΔL(Ch).

4.4. Chapter Summary

This chapter presented some comparisons between simulated and fitted profiles. It has been shown that when fitting considerations are correct, fitted parameters agreed with the simulated ones and the shape of the fitted luminosity profile, the physical quantity measured in real conditions, is similar to the simulated ones.

5. Real Data Fitting

In this chapter, the developed method is applied to fit emissivity profiles using Soft X-Rays and Bolometer luminosity data from TCABR tokamak discharges. The first analyzed discharge has stable control parameters and it was used to check this method effectiveness. The second one has a strong density increase because some gas was injected during the plasma current plateau phase.

5.1. Discharge #32726

In Figure 5-1, it is shown the plasma control parameters for discharge #32726. Both signals have not changed significantly in time range from 70ms to 90ms. Since plasma was in a quasi-stationary equilibrium condition, its emissivity profile could be evaluated. The average parameters in this case are $I_p \sim 87\ \mathrm{kA}$ and $n_e \sim 1.4\,.\,10^{19} \mathrm{electrons/m^3}$.

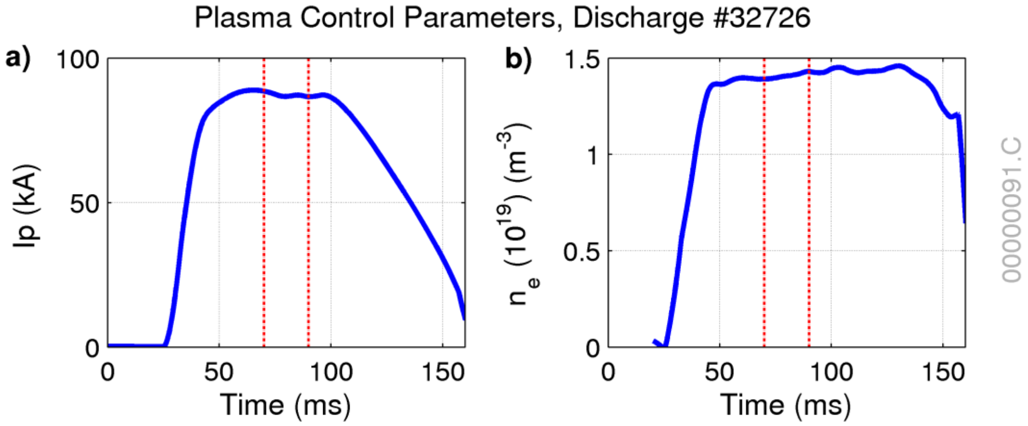

Figure 5-1: Plasma Control Parameters, Discharge 32726, 70-90ms,

a) Plasma Current and b) Electron Density

5.1.1.Soft X-ray

Measured SXR luminosity data are shown in Figure 5-2 for every 2ms in selected time interval.

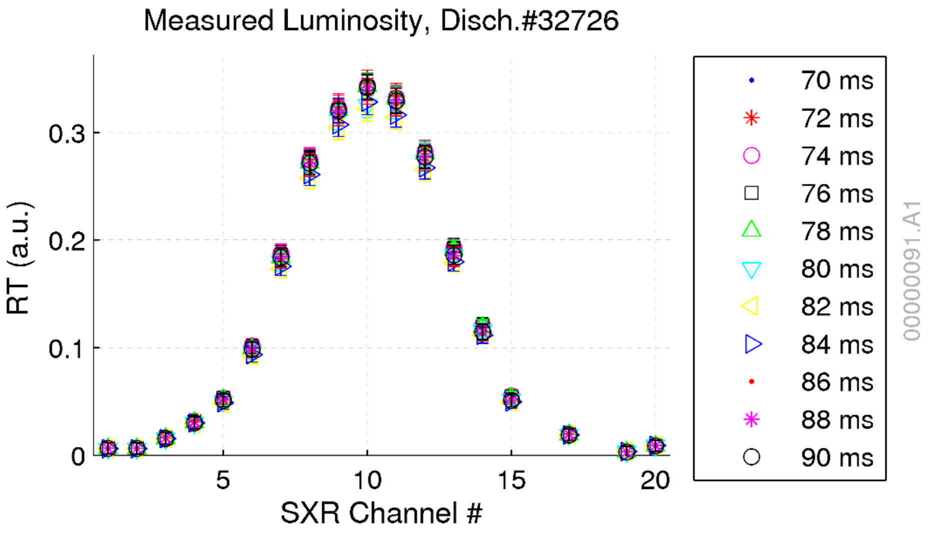

Figure 5-2: Measured SXR Luminosity Data, Discharge 32726, 70-90ms

Another way to see these measured data together is by using grid-like figures. Therefore, Figure 5-3 shows the same measured SXR luminosity data shown in Figure 5-2.

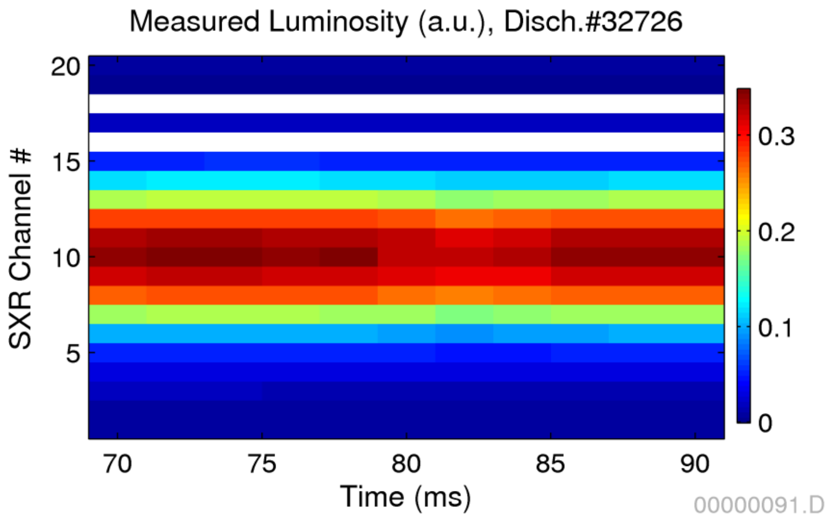

Figure 5-3: Measured SXR Luminosity Data, Discharge 32726, 70-90ms.

In last figure, channels #16 and #18 were represented in white color due to their data were not available. In addition, these channels were not used for fitting procedure. This representation in white color is adopted for all figures like this one.

5.1.1.1. Parabolic Fitting Profile

Here, Soft X-Ray luminosity data is fitted by a parabolic profile model, which is reproduced in equation 5-1 below. Considering mean values for fitted E_0 and γ parameters, in the selected time interval, we obtain the results shown in equation 5-2 and Figure 5-4:

$$E(\rho) = E_0(1 - \rho^2)^{\gamma} \tag{5-1}$$

$$\begin{aligned} E_0 &= 0.0335\ (10)\ V/cm \\ \gamma &= 9.2\ (3) \end{aligned} \tag{5-2}$$

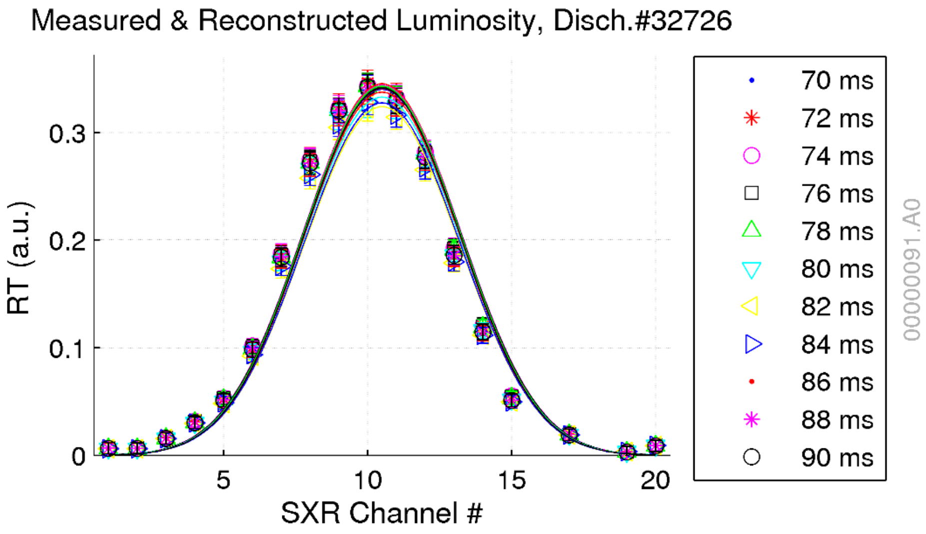

Figure 5-4: Measured and Reconstructed SXR Luminosity for a parabolic fitting profile, Discharge 32726, 70-90ms

Analyzing Figure 5-4, it is possible to realize that the measured data are above the fitted curves for low SXR channels and they are below the fitted curves for high SXR channels. It is consistent with a displacement in the vertical position that has already been simulated in section 4.3. In fact, there is a direct relation of Figure 5-4 and plot (d) in Figure 4-6 and of Figure 5-6 and plot (e) in Figure 4-6 for each time considered in this real case.

Figure 5-5 shows only reconstructed SXR data presented in Figure 5-4, and Figure 5-6 shows only fit residuals, defined as a difference between measured data and reconstructed data.

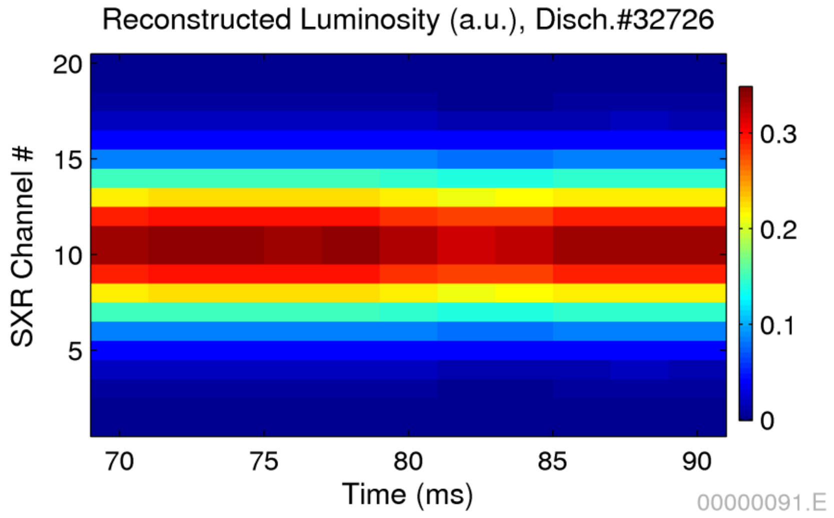

Figure 5-5: Reconstructed SXR Luminosity for a parabolic fitting profile, Discharge 32726, 70-90ms.

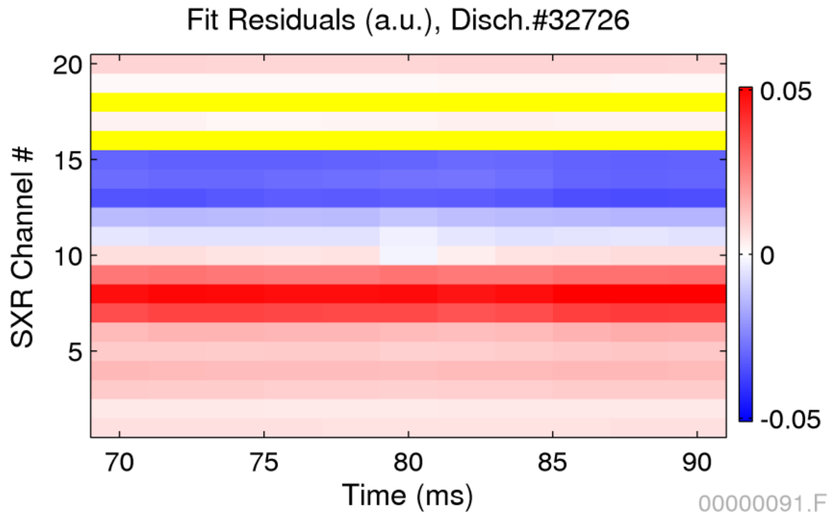

Figure 5-6: Fit Residuals SXR Luminosity for a parabolic fitting profile, Discharge 32726, 70-90ms

In last figure, channels #16 and #18 were represented in yellow color due to their data were not available. This representation is adopted for all figures like this one.

5.1.1.2. Parabolic Fitting Profile, including vertical displacement

Once a vertical position displacement has been found in last fitting procedure, ‘z_0’ was included as a free fitting parameter – it would determine the real plasma vertical position. Then, the new results are shown in equations 5-3, Figure 5-7, Figure 5-8 and Figure 5-9.

$$E_0 = 0.0350\ (10)\ V/cm$$
$$\gamma = 9.6\ (3)$$
$$z_0 = -0.65\ (6)\ cm \tag{5-3}$$

According to equations 5-3, there is a difference in expected plasma vertical position about $-0.65\mathrm{cm}$. Since parameters E_0 and γ changed a little ($< 4\%$), reconstructed luminosity curve has not changed significantly. However, Figure 5-7 shows that current fit residuals are lower than it was in previous case, shown in Figure 5-6. Note that both figures use the same scales.

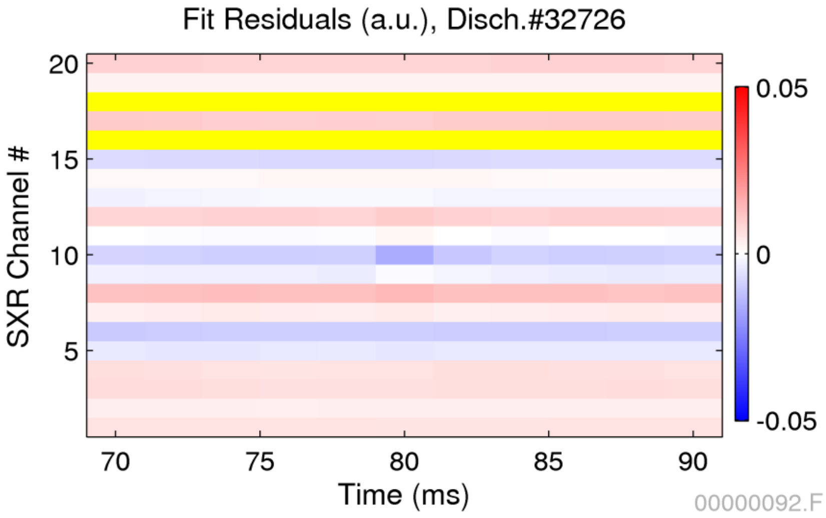

Figure 5-7: Fit Residuals SXR Luminosity for a parabolic fitting profile w/ vertical displacement, Discharge 32726, 70-90ms.

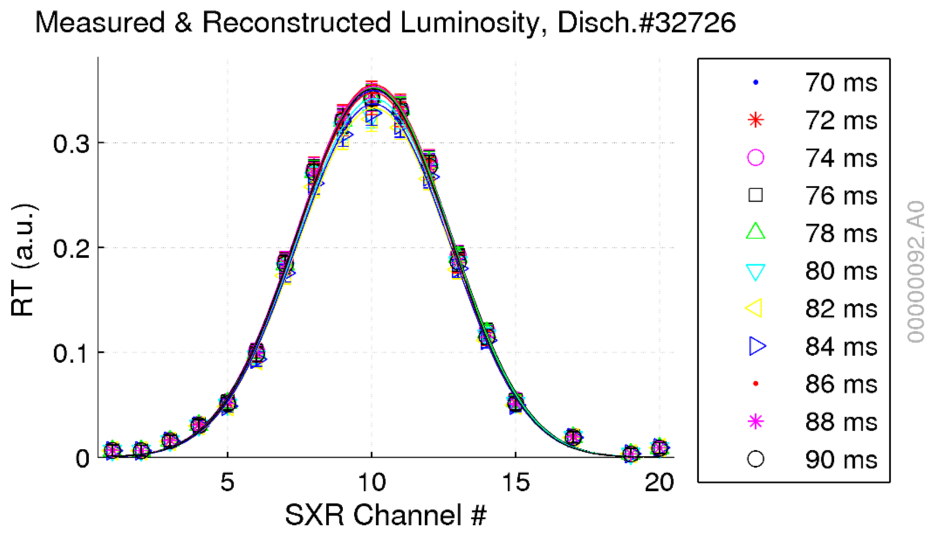

Figure 5-8: Measured and Reconstructed SXR Luminosity for a parabolic fitting profile w/ vertical displacement, Discharge 32726, 70-90ms

Additionally, this fitting procedure resulted in $\chi_R^2 \sim 1.2$. Comparing it to the previous one, which resulted in $\chi_R^2 \sim 8.0$, we can conclude that this fitting is much better than the previous one.

The reconstructed emissivity profile from equation 5-3 is shown in Figure 5-9.

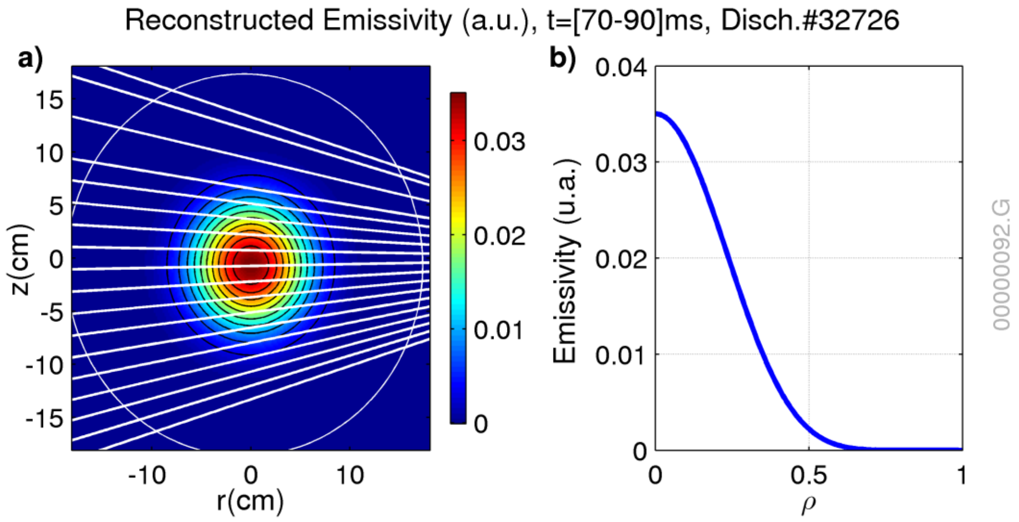

Figure 5-9: Reconstructed SXR Emissivity for a parabolic fitting profile w/ vertical displacement, Discharge 32726, 70-90ms.

5.1.1.3. Gaussian Fitting Profile, including vertical displacement

Since last fitting resulted in a high γ ($\gtrsim 5$), meaning that measured SXR data is not close to a parabolic model, it is interesting to try a Gaussian emissivity profile, which is reproduced in equation 3-2 below:

$$E(\rho) = E_0 e^{-\frac{1}{2}\left(\frac{\rho}{\sigma}\right)^2} \tag{3-2}$$

Fitting results, including z_0 as free parameter, are shown in equations 5-4, Figure 5-10 and Figure 5-11.

$$\begin{gathered} E_0 = 0.0363\ (11)\ V/cm \\ \sigma = \ 0.214\ (3) \sim 3.85\ (6)\ cm \\ z_0 = \ -0.64\ (6)\ cm \end{gathered} \tag{5-4}$$

Comparing equations 5-4 to previous parabolic fitting results in equations 5-3, both maximum emissivity (E_0) and vertical position (z_0) are compatible. This is a desired result since measured luminosity data are the same. The difference from previous case is that the Gaussian profile fitting returns the emissivity profile width that is $r_\sigma = \sigma a_0 \sim 0.21 \times 18\ cm \sim 3.8\ cm$. The reconstructed Gaussian emissivity profile is shown in Figure 5-12.

The reconstructed Gaussian profile width matches the position of the plasma rational surface $q = 1$, that bounds where most part of plasma energy is accumulated [37, 25]. Indeed, due to the beryllium filter, Soft X-Ray diagnostic only measures high energy emissions that come, mainly, from the central part of the plasma, making emissivity profile to be more concentrated at the plasma core (low ρ region).

An important aspect of the emissivity profile width is its relation to the beryllium filter used in Soft X-Ray diagnostic. This filter prevents low energy plasma emissions, from high ρ, to be measured by Soft X-Ray sensors and the energy cut off depends on filter thickness which exactly value is unknown.

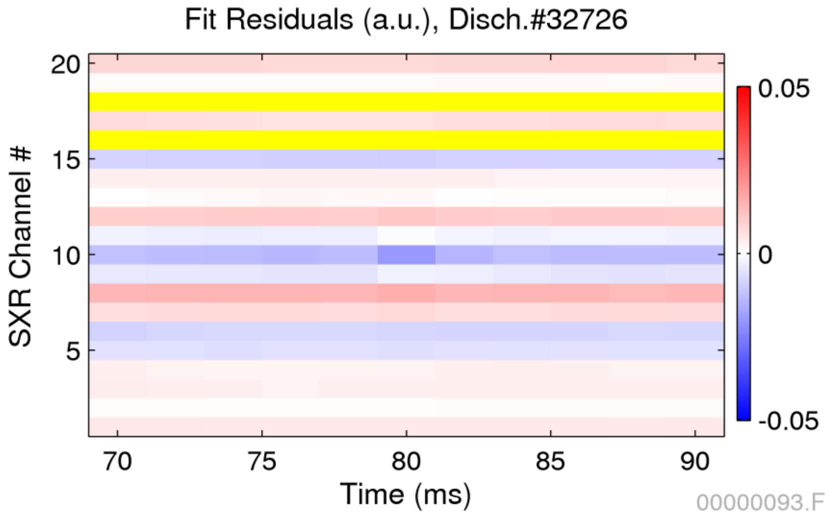

Figure 5-10: Fit Residuals SXR Luminosity for a Gaussian fitting profile w/ vertical displacement, Discharge 32726, 70-90ms.

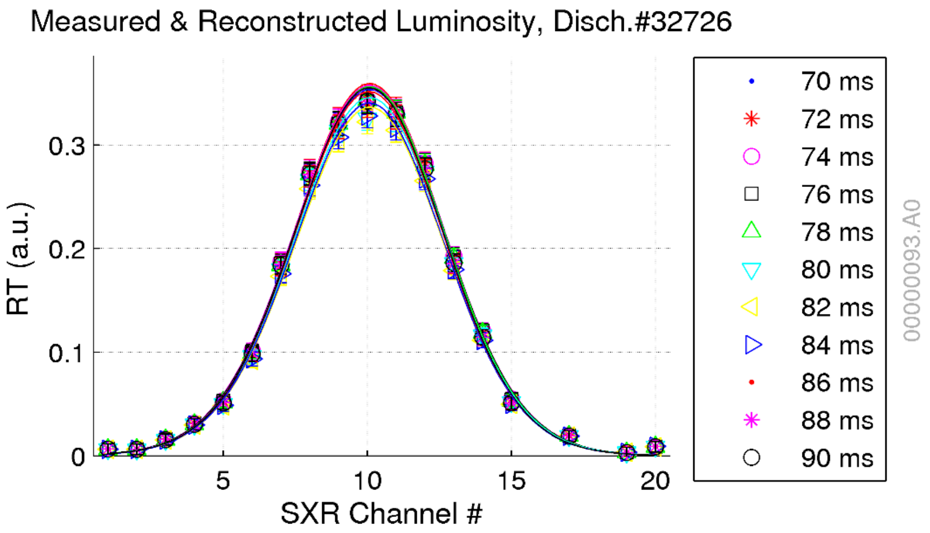

Figure 5-11: Measured and Reconstructed SXR Luminosity for a Gaussian fitting profile w/ vertical displacement, Discharge 32726, 70-90ms.

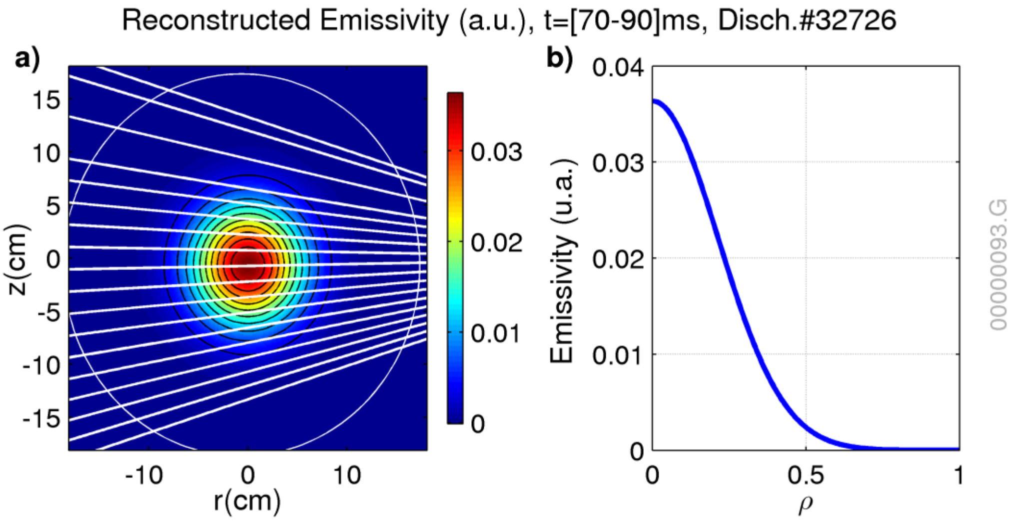

Figure 5-12: Reconstructed SXR Emissivity for a Gaussian fitting profile w/ vertical displacement, Discharge 32726, 70-90ms.

5.1.1.4. Bessel type Fitting Profile, including vertical displacement

Another emissivity profile model coded was Bessel based type. This profile model is reproduced in equation 3-4 below.

$$E(\rho) = \sum_R E_R . J_R(\rho) \qquad 3\text{-}4$$

In this case, fitting were done for all six possible maximum R, including z_0 as free parameter. Results are compiled on Table 5-1.

R	E_1	E_2	E_3	E_4	E_5	E_6	z_0 (cm)	χ_R^2
1	0.0072	-	-	-	-	-	0.03	108
2	0.0105	0.0122	-	-	-	-	-0.61	29
3	0.0107	0.0140	0.0089	-	-	-	-0.65	1.1
4	0.0108	0.0141	0.0089	0.0020	-	-	-0.64	0.7
5	0.0109	0.0141	0.0085	0.0023	-0.0015	-	-0.64	0.6
6	0.0106	0.0141	0.0092	0.0001	0.0007	-0.0044	-0.64	0.3

Table 5-1: Results for Bessel fitting

Looking at Table 5-1, it is possible to see that the χ_R^2 reduction is less important when the considered roots are above 3. Moreover, if we consider that higher R, from 4 to 6, has small E_4 coefficients, we can choose the Bessel 3 roots model for this case. The results are transcript to equation 5-5:

$$\begin{aligned} E_1 &= 0.01067\ (15)\ V/cm \\ E_2 &= 0.1395\ (3)\ V/cm \\ E_3 &= 0.0089\ (6)\ V/cm \\ z_0 &= -0.65\ (6)\ cm \end{aligned} \tag{5-5}$$

The comparison between the measured and fitted Luminosity data for this emissivity model is presented in Figure 5-13 and the correspondent emissivity profile in Figure 5-14.

The main restriction when using Bessel profiles is the non-monotonicity in some numerical solutions. This case shows, in Figure 5-14, that emissivity profile has a small bump when $0.6 < \rho < 1$. This mathematical solution does not correspond to a physical situation.

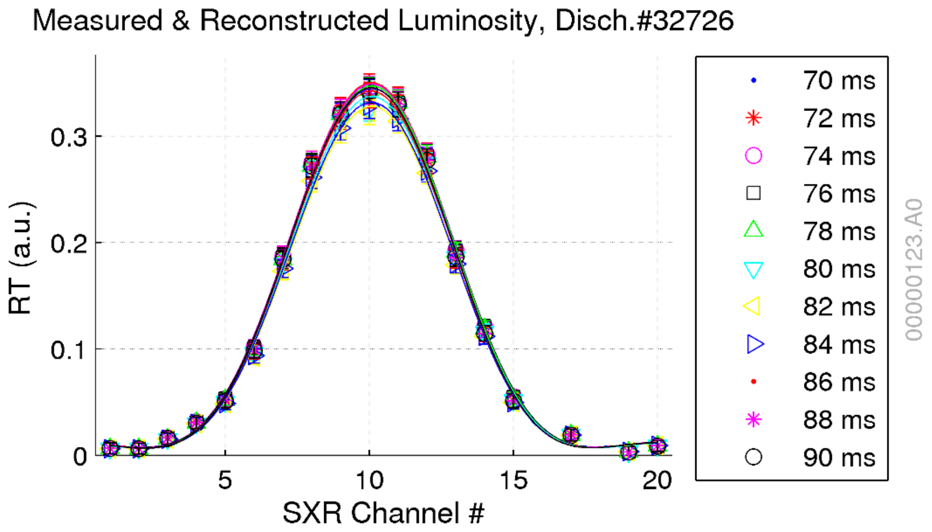

Figure 5-13: Measured and Reconstructed SXR Luminosity for a 3 roots Bessel fitting profile w/ vertical displacement, Discharge 32726, 70-90ms.

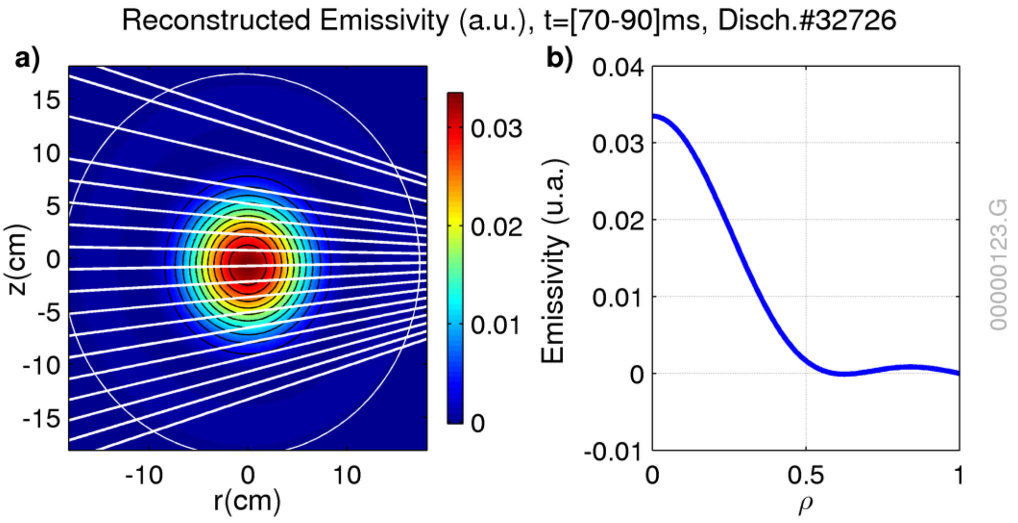

Figure 5-14: Reconstructed SXR Emissivity considering a 3 roots Bessel emissivity model with vertical displacement, Discharge 32726, 70-90ms.

Thus, we consider that the Gaussian profile is the best solution in this diagnostic.

5.1.2.Bolometer

In the Bolometer case, measured data, for every 2ms in 70-90ms time interval, are represented in Figure 5-15 and Figure 5-16. Notice that channels #9, #11 and #24 are turned off since their measured values indicate some kind of hardware failure.

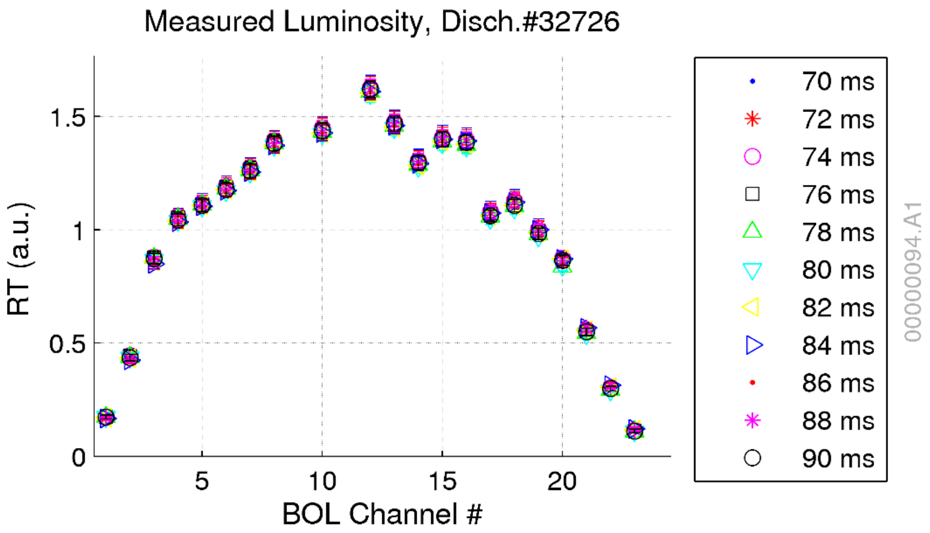

Figure 5-15: Measured Bolometer Luminosity Data, Discharge 32726, 70-90ms.

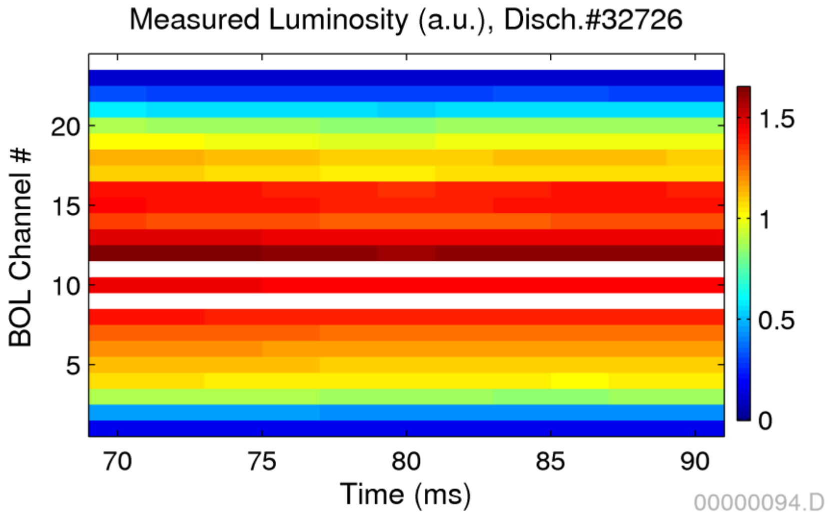

Figure 5-16: Measured Bolometer Luminosity Data, Discharge 32726, 70-90ms

Special attention must be paid to this experimental data since luminance is non-monotonic. This is, probably, due to the Bolometer hardware may have different electronic responses among channels.

5.1.2.1. Parabolic Fitting Profile

Using a parabolic profile fit, we could get results shown in equations 5-6, Figure 5-17 and Figure 5-18.

$$E_0 = 0.0540\ (6)\ V/cm$$
$$\gamma = 0.583\ (14) \tag{5-6}$$

At first, looking at Figure 5-17 and Figure 5-18, a radial position displacement can be supposed.

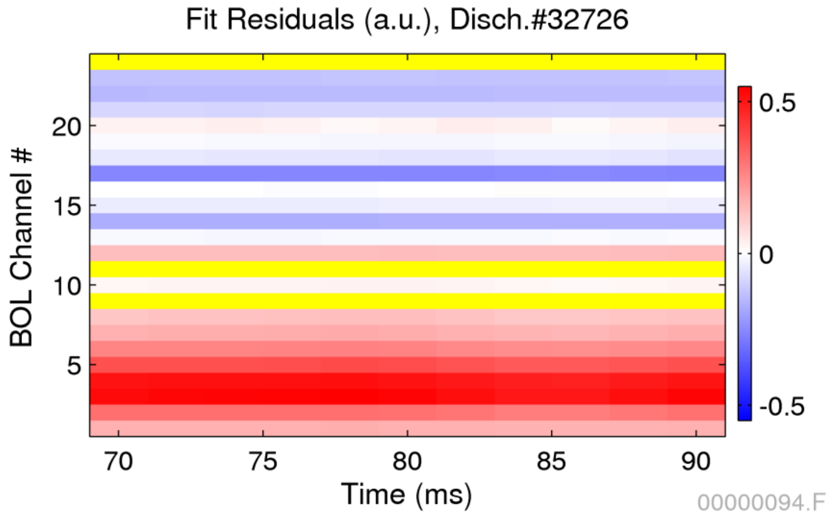

Figure 5-17: Fit Residuals Bolometer Luminosity for a parabolic fitting profile, Discharge 32726, 70-90ms.

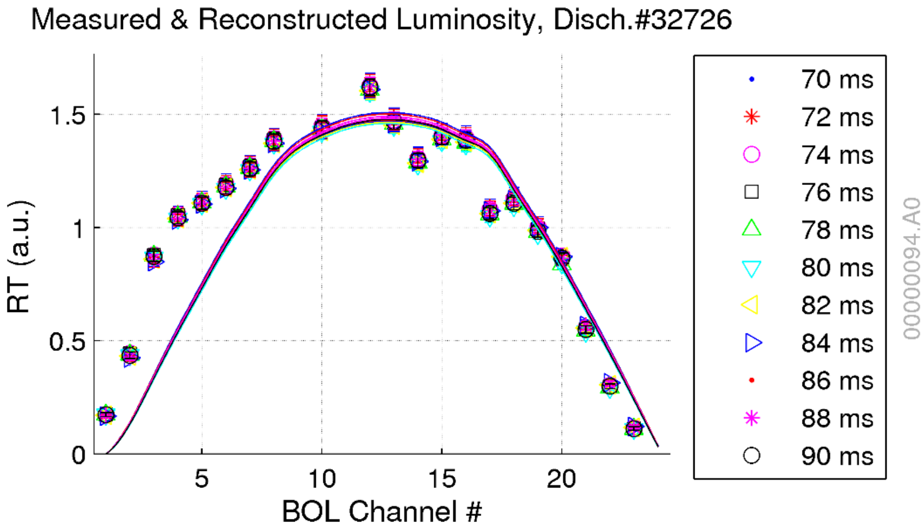

Figure 5-18: Measured and Reconstructed Bolometer Luminosity for a parabolic fitting profile, Discharge 32726, 70-90ms

5.1.2.2. Parabolic Fitting Profile, including radial displacement

Once a radial position displacement was found in last fitting procedure, a new fit was done where, $'r_0'$ was included as a fitting free. Then, new results are shown in equations 5-7, Figure 5-19 and Figure 5-20.

$$\begin{aligned} E_0 &= 0.0517\ (6)\ V/cm \\ \gamma &= 0.360\ (11) \\ z_0 &= -1.64\ (3)\ cm \end{aligned} \tag{5-7}$$

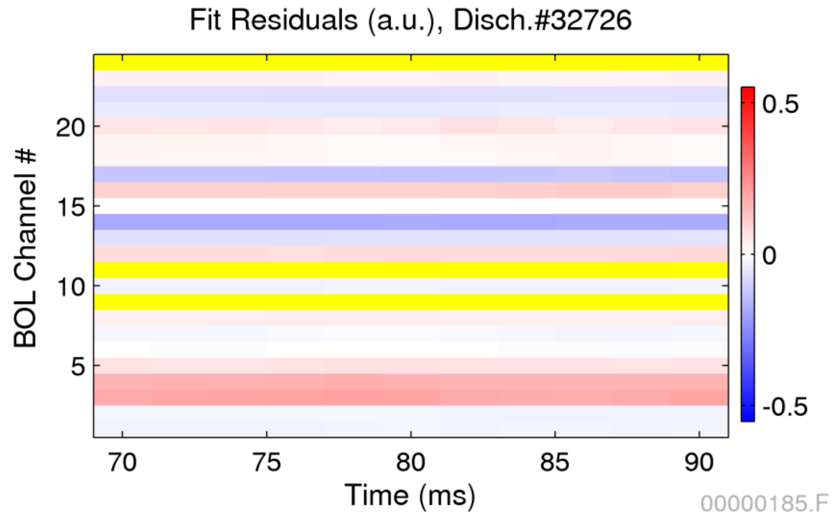

Figure 5-19: Fit Residuals SXR Luminosity for a parabolic fitting profile w/ horizontal displacement, Discharge 32726, 70-90ms.

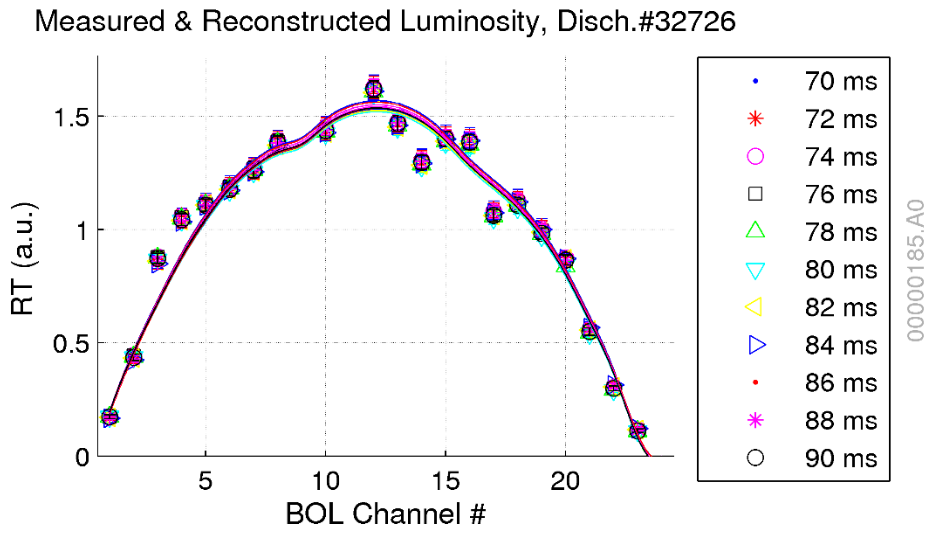

Figure 5-20: Measured and Reconstructed SXR Luminosity for a parabolic fitting profile w/ horizontal displacement, Discharge 32726, 70-90ms

According to equations 5-7, there is a difference in expected plasma horizontal position about -1.64 cm and parameter γ has changed significantly ($\sim 38\%$). Figure 5-19 and

Figure 5-20 show that fit residuals are lower than previous case but, as expected, fitting process could not handle existing experimental divergence.

Figure 5-20 shows that some channels, like #3, #4, #14 and #17, still have high errors. As already mentioned, this is probably a hardware fault. Due to this fault, the reconstructed emissivity profile may be incorrect and the emissivity parameters presented in equation 5-7 should not be taken as very confident result. So, reconstructed emissivity will not be shown. Additionally, this fitting procedure resulted in a $\chi_r^2 \sim 15.3$ – meaning that this fitting was not good enough.

5.2. Discharge #28360

Discharge #28360 was chosen because it shows how Soft X-Ray parameters change during an electron density increase due to some extra hydrogen gas injection.

Figure 5-21 shows this discharge plasma control parameters. Evaluated time interval ranges from 50ms to 100ms, where $I_p \sim 87\ \text{kA}$.

This time range was divided in three small intervals, according to electron density condition:

a) From 50 to 60ms, when electron density was $\sim 1.13 \,.\, 10^{19}\ e/m^3$;
b) From 60 to 76ms, when electron density increased up to $\sim 1.84 \,.\, 10^{19}\ e/m^3$;
c) From 78 to 100ms, when electron density decreased to $\sim 1.30 \,.\, 10^{19}\ e/m^3$.

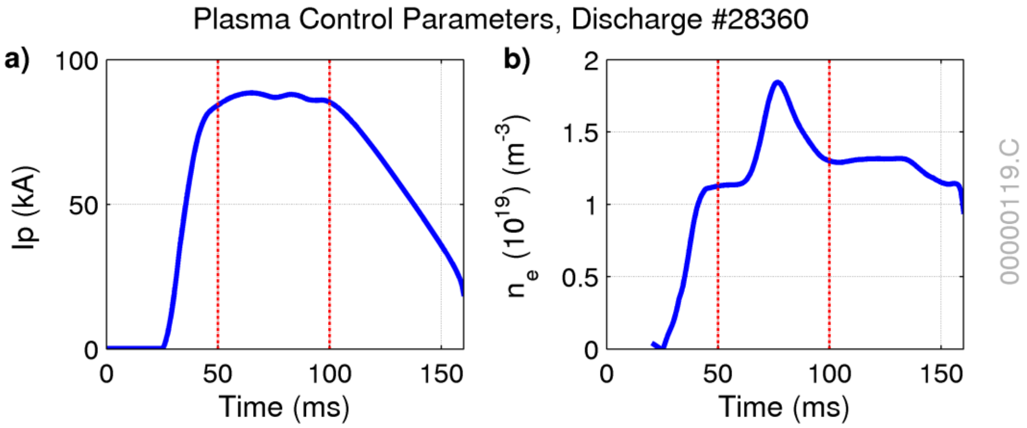

Figure 5-21: Plasma Control Parameters, Discharge 28360, 50-100ms,

a) Plasma Current (I_p) and b) Electron Density (n_e).

5.2.1.Soft X-Rays

In Figure 5-22, measured Soft X-Rays data is shown for every 1ms in chosen time interval.

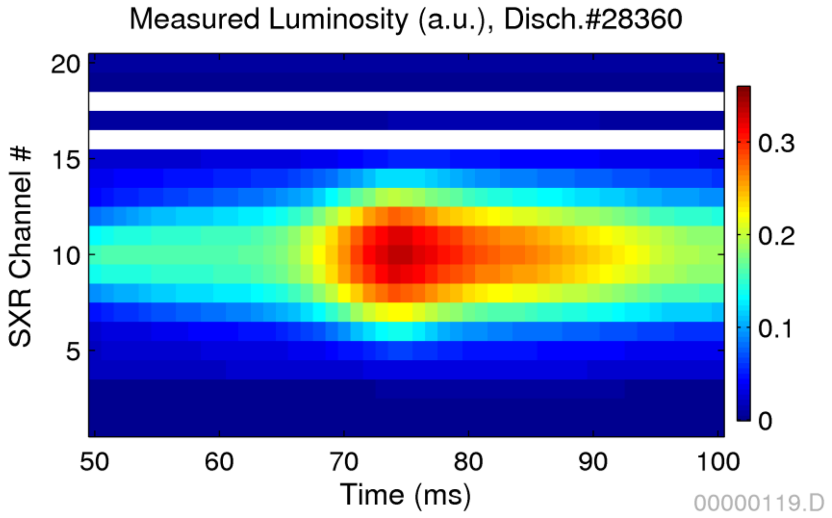

Figure 5-22: Measured Soft X-Rays Luminosity Data, Discharge 28360, 50-100ms.

Fitting these Soft X-Rays data to a Gaussian plasma emissivity profile model, including z_0 as a free parameter, gives results shown in Figure 5-23.

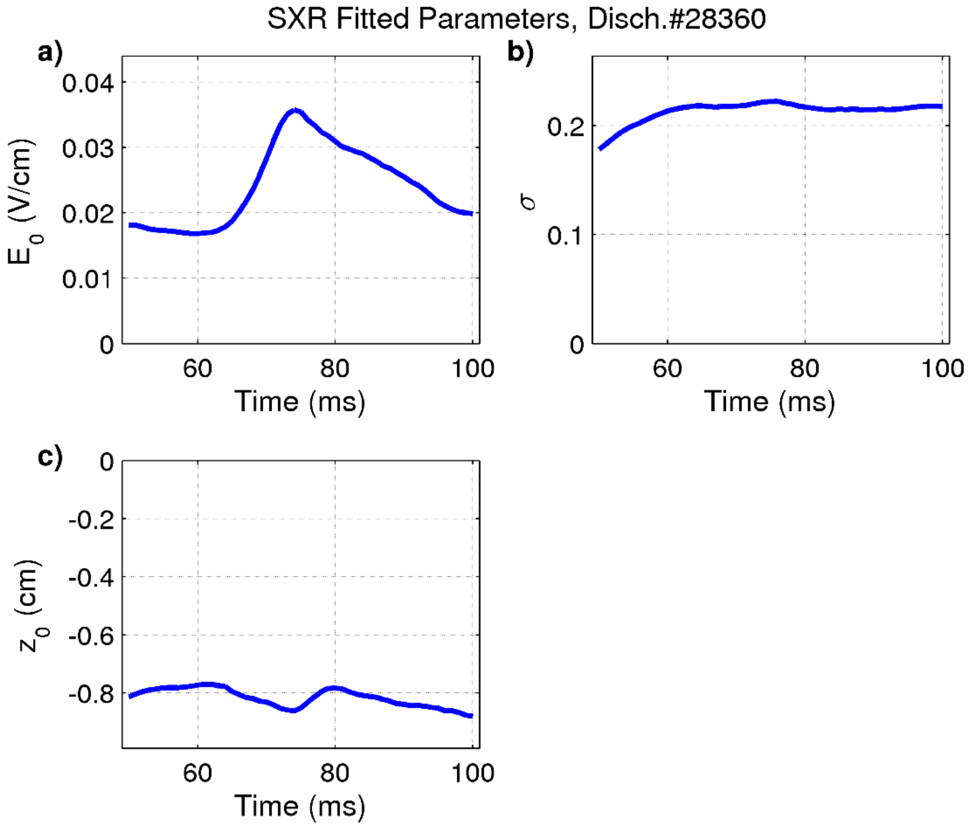

Figure 5-23: Fitted Soft X-Rays Parameter Evolution, w/ vertical displacement, Discharge 28360, 50-100ms.

These results can be interpreted as:

a) z_0 is $\sim -8\,mm$, with small deviation in the whole considered time interval (variation lower than $0.5\,mm$ in the plasma vertical position). This is considered a negligible change.

b) E_0 curve shape is like n_e one. Although there is a delay $\sim 3.0\,ms$ between both maxima, with E_0 maximum happening after n_e one.

c) σ is ~ 0.22 $(\sim 4.0\,cm)$ during electron density increase and decrease phases. Changes in σ are considered negligible ~ 0.006 $(\sim 1.1\,mm)$.

In Figure 5-24, we have the comparison between SXR input data to adjusted ones. The differences are very small indicating that these fits are suitable to describe the SXR emissivity evolution. The comparison between the measured and reconstructed SXR emissivity profiles were separated in three figures. Firstly, Figure 5-25 shows the plateau phase before the extra gas injection (from 50 to $60\ ms$). Figure 5-26 shows the rising phase (from 60 to $76\ ms$) and the decreasing phase is shown in Figure 5-27 (from 76 to $100\ ms$).

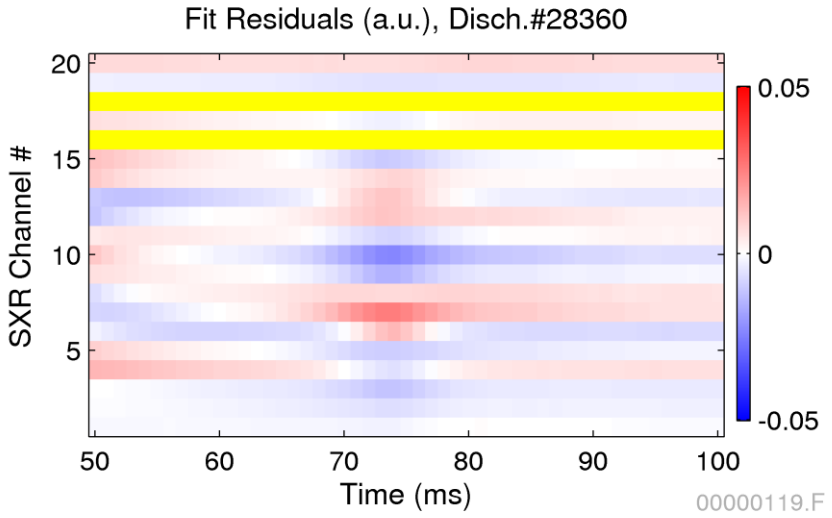

Figure 5-24: Fit Residuals Soft X-Rays Luminosity for a Gaussian fitting profile w/ vertical displacement, Discharge 28360, 50-100ms.

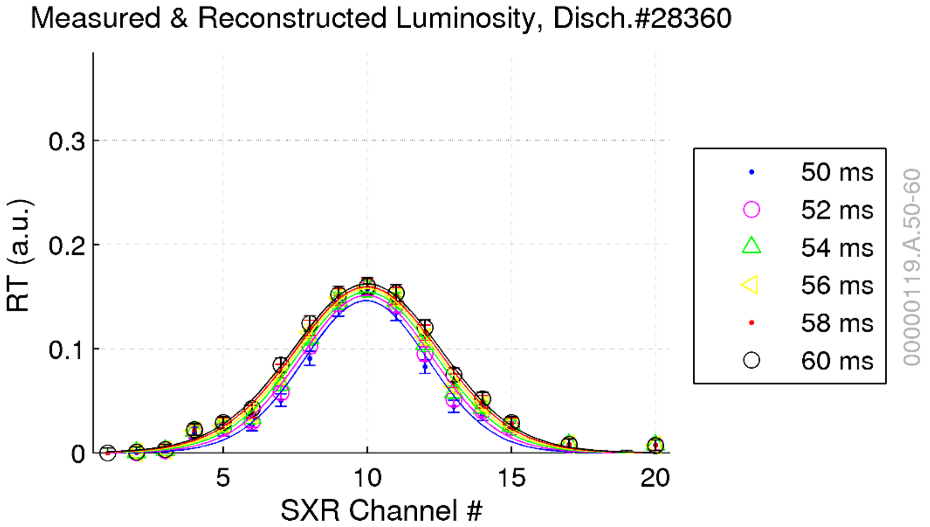

Figure 5-25: Measured and Reconstructed Soft X-Rays Luminosity for a Gaussian fitting profile w/ vertical displacement, Discharge 28360, 50-60ms.

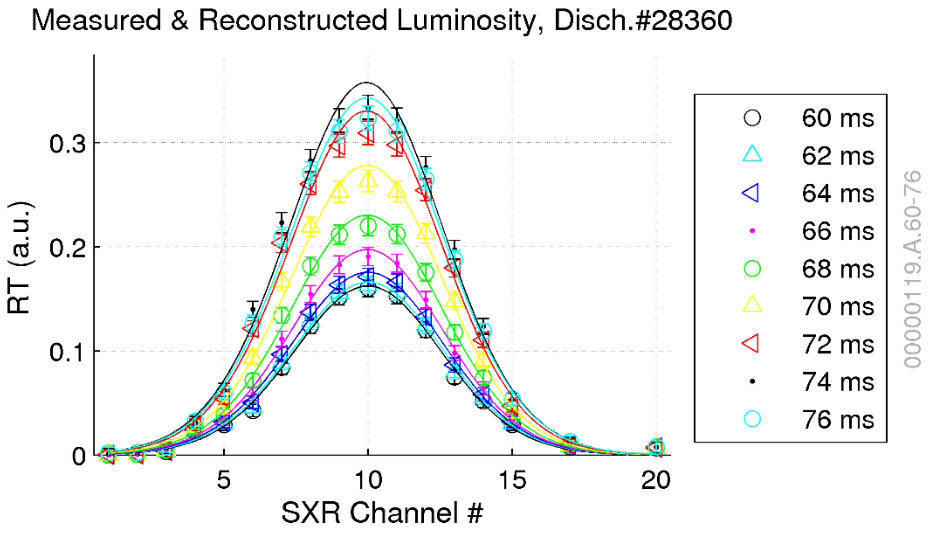

Figure 5-26: Measured and Reconstructed Soft X-Rays Luminosity for a Gaussian fitting profile w/ vertical displacement, Discharge 28360, 60-76ms.

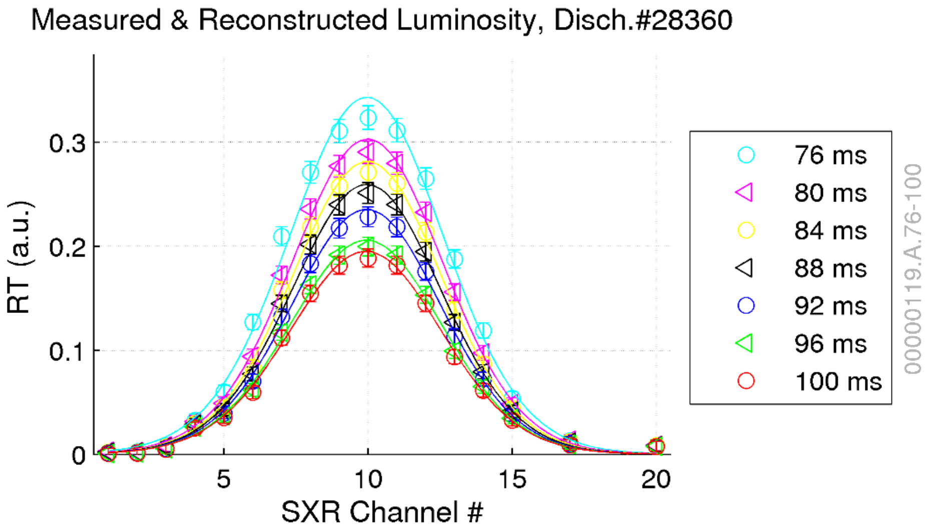

Figure 5-27: Measured and Reconstructed Soft X-Rays Luminosity for a Gaussian fitting profile w/ vertical displacement, Discharge 28360, 76-100ms.

In this case, reconstruct emissivity will not be shown because it changes for each specific time, as it can be seen in Figure 5-23.

5.3. Chapter Summary

In this chapter, Soft X-Rays and Bolometer experimental data were used to reconstruct plasma emissivity profiles. Some data were fitted to different profile types in order to find the most adequate one.

In discharges #32726 and #28360, the Soft X-Ray data were best fitted by a Gaussian emissivity profile ($\sigma \sim 0.21$), while the Bolometer data were well fitted by a parabolic emissivity profile ($\gamma \sim 0.36$), in the first discharge. We have found that the Gaussian σ from reconstructed Soft X-Ray emissivity is close to the position of plasma rational surface $q = 1$.

6. Conclusion

This work described the implementation of a computational method to reconstruct the equilibrium emissivity profiles for optical diagnostics in TCABR tokamak. These profiles are useful to study the equilibrium characteristics and their evolution in plasma discharges.

The results presented in this work show that this method is suitable to estimate equilibrium emissivity profiles using the measured luminance data from Bolometer and Soft X-Ray diagnostics in almost stationary plasma discharges. This method also works when electron density increases smoothly during the plasma current plateau phase of TCABR discharges. Moreover, it can identify position displacements that are present in experimental data. The obtained result is checked by adequacy of fit residuals.

The main positive aspect of this method is the avoidance of statistical issues usually present in unfolding procedures, especially when considering experimental data with large uncertainties. Indeed, the reconstructed equilibrium emissivity profiles of ohmic discharges are physically plausible once they are smooth, monotonic, and go to zero at the plasma border.

On the other hand, the main limitation of this method is the requirement of an emissivity model type. However, the selection of the emissivity model type is, indeed, an interesting way to impose some physical constrains and to include previous knowledge in the reconstruction procedure. For instance, the Gaussian and the Parabolic-in-Law profiles are always positive and decreases monotonically with the radial position, two characteristics that are physically expected in equilibrium emissivity profiles. When considering an almost free emissivity model, like high order Bessel model, nonphysical results with eventually negative emissivity or bumps in the plasma edge region may be obtained.

We found that typical Soft X-Ray diagnostic data is properly fitted by Gaussian profiles while Bolometer data is better fitted by parabolic ones. Moreover, the beryllium filter used in Soft X-Ray diagnostic is such that the dispersion parameter (σ) of fitted profile is similar to the radial position estimated from the inversion radius of the sawteeth (q=1). On top of that, the parameters evolution during the plasma current plateau phase in perturbed discharges may allow getting relevant information about the perturbation effect in plasma characteristics.

An important aspect that can be derived from the typical emissivity profiles is the complementarity of Soft X-Ray and Bolometer diagnostics. Indeed, Soft X-Ray diagnostic is able to measure radiation from central part of plasma, which is hotter compared to border areas due to the beryllium filter that blocks low energy radiation. On the other hand, Bolometer receives radiation from all plasma – it has no radiation filter – and emissivity is high up to plasma border.

The reconstruction of the equilibrium emissivity profile is a necessary step to evaluate the magnetic displacement produced by macroscopic plasma instabilities (MHD modes). These instabilities lead to strong oscillations in the measured luminescence of both soft X-ray and bolometer diagnostics [37, 25]. The relation between the magnetic displacement, ξ, and the profile modification δ_x produced by these instabilities is given by $\delta_x = |\nabla_x|.\xi$, where ∇_x is the radial gradient of the equilibrium emissivity. Therefore, the emissivity gradient modulus of each diagnostic indicates its sensibility to MHD plasma perturbations.

By considering the typical emissivity profiles obtained in this work it is possible to estimate the profile of the emissivity gradient for both diagnostics. These profiles are shown in Figure 6-1 and Figure 6-2, in which the marks indicate the typical radial position of the magnetic surfaces with q=1 (green), q=2 (red) and q=3 (blue).

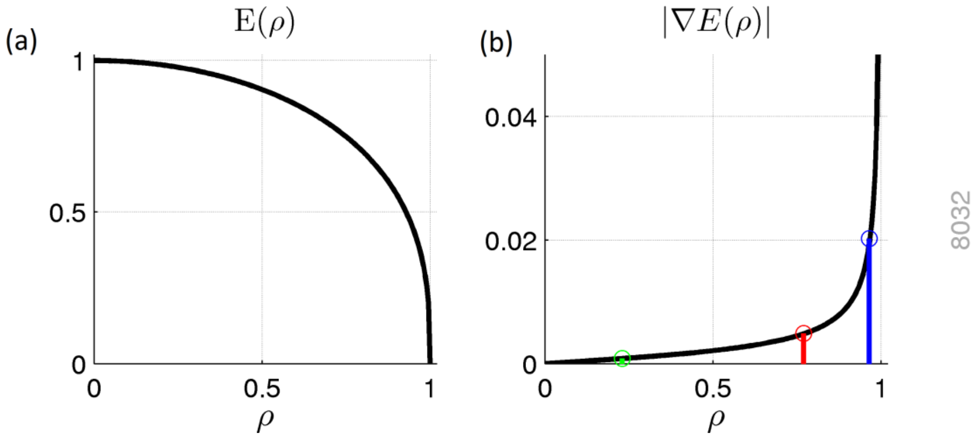

Figure 6-1: (a) Bolometer normalized typical parabolic emissivity profile ($\gamma = 0.35$) and (b) Its respective gradient.

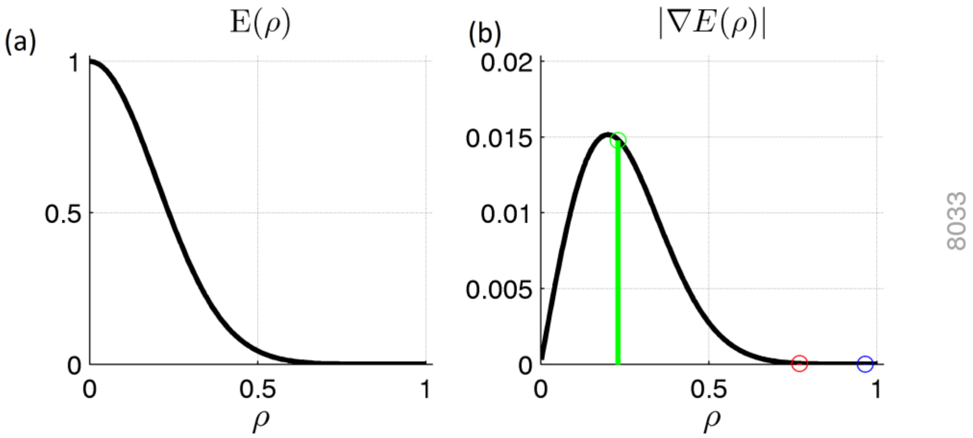

Figure 6-2: (a) Soft X-Ray normalized typical Gaussian emissivity profile ($\sigma = 0.2$) and (b) Its respective gradient.

As it can be seen in Figures Figure 6-1 and Figure 6-2, the gradient of the Bolometer emissivity is more pronounced at the high ρ, while for the Soft X-Ray the maximum gradient is located closer to the plasma core, making the Bolometer a suitable diagnostic to observe the MHD perturbations produced by the magnetic islands, that appear at q=2 and q=3 [25], while the Soft X-Ray is more adequate to observe the sawteeth and its precursors, that are located at q=1 [37, 25].

It is worth to mention that the developed method was adapted to reconstruct the emissivity profile of Carbon impurity spectral lines (C-III and C-VI) measured by a different diagnostic in TCABR. Moreover, a further modification in the method allows estimating the poloidal and toroidal profiles of plasma rotation by the projections of the Doppler Shift line integrated signal. The results obtained with this modified version of the code were included in the paper '*Investigation of rotation at the plasma edge in TCABR'* published at Nuclear Fusion, **55**, 093001, by J.H.F. Severo *et al.*, in 2015 [38]. The modifications we made on the fitting code to allow dealing with plasma rotation measurements are presented in Appendix A – Application of the emissivity reconstruction method in plasma rotation studies.

7. References

[1] O. Helene, V.R. Vanin, Z.O. Guimarães-Filho, C. Takiya, *Variances, covariances and artifacts in image deconvolution*. Nuclear Instruments & Methods in Physics Research, Section A, **580** (2007) 1466.

[2] M. Morháč, *Deconvolution methods and their applications in the analysis of image γ-ray spectra*, Nuclear Instruments & Methods in Physics Research, Section A, 559 (2006) 119.

[3] I. C. Nascimento, *et al.*, *Preliminary results from the TCABR tokamak*. IN: 1999 IAEA Technical Committee Meeting on Research Using Small Fusion Devices, 1999.

[4] W. P. de Sá, *Tokamak TCABR: acquisition system, data analysis, and remote participation using MDSplus*. Fusion Engineering and Design **87** (2012) 2199.

[5] W. P. de Sá, *Reconstrução do equilíbrio no tokamak TCABR*. Tese (Doutorado em Física), Universidade de São Paulo, 1996.

[6] A. M. M. Fonseca, *Emissão eletrociclotrônica no tokamak TCABR: um estudo experimental*. Tese (Doutorado em Física), Universidade de São Paulo, 2005.

[7] I.C. Nascimento, *et al.*, *Preliminary results of the TBR Small Tokamak*. In: Spring College On Fusion Energy - ICTP-IAEA, 1981, Trieste, Italy: ICTP-IAEA, 1981, p. 59.

[8] TCABR Wiki, available at <http://tcabrcl.if.usp.br/tcabrWiki/index.php/Main_Page>, accessed in Jun 19, 2017.

[9] K. Ikeda, *Progress in the ITER physics basis*, Nuclear Fusion **47** (2007) 1.

[10] H. Grad, H. Rubin, *Hydromagnetic Equilibria and Force-Free Fields*. Proceedings of the second UN Conf. on the Peaceful Uses of Atomic Energy, Vol. 31, Geneva: IAEA p. 190, 1958.

[11] J. D. Callen, *Fundamentals of Plasma Physics*, University of Wisconsin, Madison, 2006.

[12] P. Bellan, *Fundamentals of Plasma Physics*, Cambridge University Press, London, 2006

[13] V. D. Shafranov, *Equilibrium of a toroidal pinch in a magnetic field*, Soviet Atomic Energy, **13(6)** (1963) 1149.

[14] Y. Peysson, F. Imbeaux, *Tomography of the fast electron bremsstrahlung emission during lower hybrid current drive on Tore Supra*. Review of Scientic Instruments **70** (1999) 3987.

[15] H. J. Hartfusset. *et al.*, *Heterodyne methods in millimeter wave plasma diagnostics with applications to ECE, interferometry and reflectometry*, Plasma Phys. Control. Fusion **39** (1997) 1693.

[16] K. Miyamoto, *Fundamentals of Plasma Physics and Controlled Fusion*, NIFS-PROC-88, third ed., 1991.

[17] G. Bekefi, *Radiation Process in Plasma*, John Wiley & Sons, first ed., 1966.

[18] R.J. Goldston, P.H. Rutherford, *Introduction to Plasma Physics*, IOP Publishing, first ed., Reprinted, 2000.

[19] C. Breton, C. de Michelis, M. Mattioli, *Ionization equilibrium and radiative cooling of a high temperature plasma*, Journal of Quantitative Spectroscopy and Radiative Transfer, **19(3)**, (1978) 367.

[20] T. Odstrčil, *Study of visible plasma radiation by high resolution spectroscopy at additional plasma heating by neutral beams injection on the COMPASS tokamak*. Diploma Thesis, Czech Technical University in Prague, 2012.

[21] S. Morita, *et. al.*, *Zeff measurements in ATF using visible bremsstrahlung*, ORNL, TM-11737, 1991.

[22] A.P. Vasiliev, *et al.*, Nuclear Fusion, supplement, part **2**, (1962) 655.

[23] D. C. Taborda, *MHD equilibrium in tokamaks with reversed current density*. Dissertação (Mestrado em Física), Universidade de São Paulo, 2012.

[24] V. Bellintani Jr., *Diagnóstico bolométrico no TCABR*. Tese (Doutorado em Física), Universidade de São Paulo, 2005.

[25] V. C. Theodoro, *Estudo espectral das instabilidades MHD no tokamak TCABR*. Dissertação (Mestrado em Física), Universidade de São Paulo, 2013.

[26] C. de Michelis, M. Mattioli, *Soft X-ray spectroscopic diagnostics of laboratory plasmas*, Nuclear Fusion **21** (1981) 677.

[27] R.M.O. Galvão, *et al.*, *Report on recent results obtained in TCABR*, IOP Journal of Physics: Conference Series **591** (2015) 012001.

[28] O. C. N. Usuriaga, *Tomografia de emissão H-alpha no tokamak TCABR*. Tese (Doutorado em Física), Universidade de São Paulo, 2006.

[29] S. Helgason, *The Radon transform*, Boston Birkhäuser, second ed., 1999.

[30] K. Bockasten, *Transformation of Observed Radiances into Radial Distribution of the Emission of a Plasma*, J. Opt. Soc. Am. **51** (1961) 943

[31] O. A. M. Helene, V. R. Vanin, *Tratamento estatístico de dados em física experimental*, Edgard Blücher, segunda ed., 1991.

[32] M.G. Kendall, A. Stuart, *The Advanced Theory of Statistics*, vol. 2, Charles Griffin and Co. Ltd., London, 1967.

[33] O.Barana, D.Mazon, Y.Peysson, *Real time algorithm for Hard X-ray treatment in a fusion reactor: local emissivity profile reconstruction*, Tore Supra Technical note (2004).

[34] Y.Peysson, *et al.*, *Tomography of the fast electron bremsstrahlung emission during lower hybrid current drive on TORE SUPRA*, Review of Scientific Instruments **10** (1999) 70.

[35] O. Barana, *et al.*, *Real-time determination of suprathermal electron local emission profile from hard X-ray measurements on Tore Supra*, IEEE Transactions on Nuclear Science, **53(3)** (2006) 1051.

[36] E. Joffrin, *et al.*, *Integrated plasma controls for steady state scenarios*, Nuclear Fusion **47** (2007) 1664.

[37] T. Fernandes, *Instabilidades MHD no tokamak TCABR*. Dissertação (Mestrado em Física), Universidade de São Paulo, 2016.

[38] J.H.F. Severo, *et al.*, *Investigation of rotation at the plasma edge in TCABR*, Nuclear Fusion **55** (2015) 093001.

[39] J.H.F. Severo, *et al.*, *Temporal behaviour of toroidal rotation velocity in the TCABR tokamak*, Nuclear Fusion **49** (2009) 115026.

[40] R.W. Boyd, *Radiometry and the detection of optical radiation*, New York, John Wiley & Sons, second ed., 1983.

8. Appendix A – Application of the emissivity reconstruction method in plasma rotation studies

The computational tools developed in this work for emissivity reconstruction were adapted to be used in a plasma rotation study made in TCABR, which results were published at Nuclear Fusion **55** (2015) 093001 [38]. This application required several modifications in the base code developed for the Bolometer and Soft X-Ray signals.

In order to study the plasma rotation, the Doppler shift of selected impurity carbon lines (C_{III} - 464.74 nm and C_{VI} – 529.06 nm) is measured in both poloidal and toroidal direction by using an original spectroscopic method developed in TCABR [39].

As it can be seen in the experimental setup shown in Figure 1 of the paper, the poloidal rotation is measured in vertical line-of-sights at different radial positions of a top window of the TCABR, which is similar to the geometry used for the Bolometer. On the other hand, the toroidal rotation is measured with horizontal line-of-sights at the equatorial plane of the machine, which required the consideration of a complete different geometry.

The first result obtained using the modified version of the codes were the reconstruction of the C_{III} and C_{VI} emissivity profile, presented in Figures 7 and 8 of the paper. A modified version of the Gaussian profile was used to fit these profiles that do not have the maximum emissivity at the plasma axis:

$$E(\rho) = E_M e^{-\frac{1}{2}\left(\frac{\rho-\rho_M}{\sigma}\right)} \qquad \text{8-1}$$

where E_M is the maximum emissivity which occurs at $\rho = \rho_M$, and σ is the radial dispersion of the emissivity peak. The emissivity of the C_{III} spectral line is mainly concentrated at the plasma edge, with the maximum emissivity at $\frac{r}{a} \cong \frac{14\,cm}{18\,cm}$ $(\rho_M \cong 0.75)$, while the C_{VI} emissivity is broader with the maximum at $\frac{r}{a} \cong \frac{9\,cm}{18\,cm}\,(\rho_M \cong 0.5)$.

Based on the emissivity profiles and the Doppler shift measurements, the poloidal and toroidal rotation velocities were estimated by considering that the measured Doppler signal corresponds to the line integration of the rotation velocity projection in the direction of the detector line-of-sight:

$$L = \int_l E(\rho)\vec{v} \cdot d\vec{l} \qquad 8\text{-}2$$

By considering a third degree polynomial profile for the plasma velocity magnitude, $V(\rho) = v_0 + v_1\rho + v_2\rho^2 + v_3\rho^3$, the free parameters v_i, $i = 0,1,2,3$, were fitted for C_{III} and C_{VI} Doppler measurements in both poloidal and toroidal directions. As the direction of the velocity is always tangential to the field surface, the inner product can be written as $\vec{v} \cdot d\vec{l} = V(\rho)\cos(\alpha)dl$, where α is the angle between the radial position and the considered line-of-sight. The results of these fits are in Figures 9 and 10 of the paper.

9. **Appendix B – Slits Optical Attenuation**

Slits attenuation for Bolometer and Soft X-Ray optical diagnostics at TCABR were calculated by V.C.Theodoro, in his Master Dissertation [25]. This reference, in its Annex B, and reference [40] provide basic definitions and equations for the radiometry study.

In this work, we defined the parameter K_α to be the slit signal attenuation for each channel due to radiation incidence angle, first used in equation 1-7. According to this definition, K_α can be calculated by equation 9-1:

$$K_\alpha = \frac{g(\varphi)}{g(0)} \qquad \text{9-1}$$

where: $g(\varphi)$ is the equation B.25 from reference [25];

$\alpha = \varphi$ is the radiation incidence angle related to the normal.

The function $g(\varphi)$ deduced in reference [25] is transcript below:

$$\begin{aligned} g(\varphi) = {} & \frac{A_f A_d cos^4\varphi}{4\pi d^2}\left[1 - \frac{D_x^2 + D_y^2 + F_x^2 + F_y^2}{6d^2} cos^2\theta \right. \\ & + (D_x^2 + F_x^2)\left(\frac{sin^2\theta + cos^2\theta}{d^2}\right) \\ & + \frac{cos^4\theta}{d^4}\left(\frac{3}{80}\left(D_x^4 + D_y^4 + F_x^4 + F_y^4\right) + \frac{1}{8}\left(D_x^2 F_x^2 + D_y^2 F_y^2\right)\right. \\ & \left. + \frac{1}{24}\left(D_x^2 D_y^2 + D_x^2 F_y^2 + F_x^2 D_y^2 + F_x^2 F_y^2\right)\right) - \frac{3cos^4\theta + sin^2\theta}{d^4} \\ & \left. \times \left(\frac{D_x^4 + F_x^4}{5} + \frac{\left(7D_x^2 F_x^2 + D_x^2 D_y^2 + F_x^2 D_y^2 + F_x^2 F_y^2 + D_x^2 F_y^2\right)}{9}\right)\right] \end{aligned} \qquad \text{9-2}$$

where: A_f is the slit area ($F_x \times F_y$);

A_d is the detector (sensor) area ($D_x \times D_y$);

d is the perpendicular distance from detector to slit;

D_x is the detector x dimension;

D_y is the detector y dimension;

F_x is the slit x dimension;

F_y is the slit y dimension;

$\theta = \varphi$ is the radiation incidence angle related to normal.

Bolometer and Soft X-Ray parameters used in function $g(\varphi)$ are presented in Table 9-1:

Parameter	Bolometer	Soft X-Rays
d (mm)	97.0	25.3
Dx (mm)	2.0	0.7
Dy (mm)	5.0	4.0
Fx (mm)	1.9	0.6
Fy (mm)	25.85	4.0

Table 9-1: Bolometer and Soft X-Ray parameters.

Figure 9-1 reproduces Figure B.4 from reference [25], where all parameters for equation 9-2 are represented. Additionally, incident radiation angle is shown.

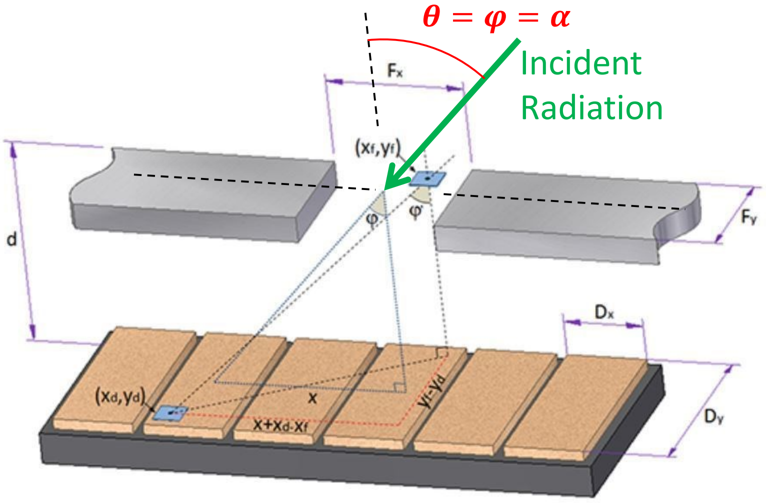

Figure 9-1: Slit, Detector (Photodiodes Array) and Incident Radiation are represented[5].

In Table 9-2 and Table 9-3, channels, radiation incidence angle and each slit attenuation (K_α) are shown for Bolometer and Soft X-Ray diagnostics, respectively.

---

[5] This figure is a reproduction of Figure B.4, Appendix B, from V.C.Theodoro Master Dissertation, reference [25]

Bolometer Ch#	φ (°)	K_α Att. Factor
1	-9.309	0.948675
2	-6.85442	0.971895
3	-4.37432	0.988474
4	-1.87769	0.997868
5	0.626094	0.999763
6	3.127484	0.994094
7	5.617003	0.981053
8	8.085443	0.961073
9	-9.309	0.948675
10	-6.85442	0.971895
11	-4.37432	0.988474
12	-1.87769	0.997868
13	0.626094	0.999763
14	3.127484	0.994094
15	5.617003	0.981053
16	8.085443	0.961073
17	-9.309	0.948675
18	-6.85442	0.971895
19	-4.37432	0.988474
20	-1.87769	0.997868
21	0.626094	0.999763
22	3.127484	0.994094
23	5.617003	0.981053
24	8.085443	0.961073

Table 9-2: Bolometer channels, radiation incidence angle and slit attenuation.

Soft X-Ray Ch#	φ (°)	K_α Att. Factor
1	-17.47	0.7918
2	-15.88	0.8278
3	-14.21	0.8619
4	-12.47	0.8934
5	-10.67	0.9219
6	-8.82	0.9467
7	-6.92	0.9672
8	-4.97	0.9831
9	-2.99	0.9939
10	-1.00	0.9993
11	1.00	0.9993
12	2.99	0.9939
13	4.97	0.9831
14	6.92	0.9672
15	8.82	0.9467
16	10.67	0.9219
17	12.47	0.8934
18	14.21	0.8619
19	15.88	0.8278
20	17.47	0.7918

Table 9-3: Soft X-Ray channels, radiation incidence angle and slit attenuation.

Attenuation factors K_α for Bolometer and Soft X-ray diagnostics are plotted in Figure 9-2 and Figure 9-3, respectively. Note that Bolometer diagnostic has 3 different slits.

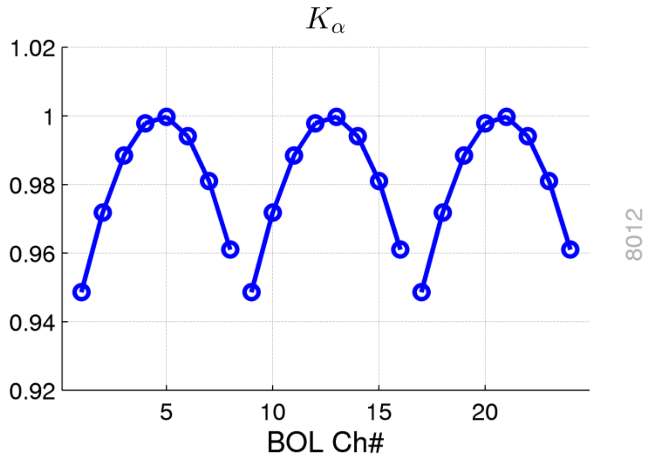

Figure 9-2: Bolometer Slit Attenuation (K_α) by Channel

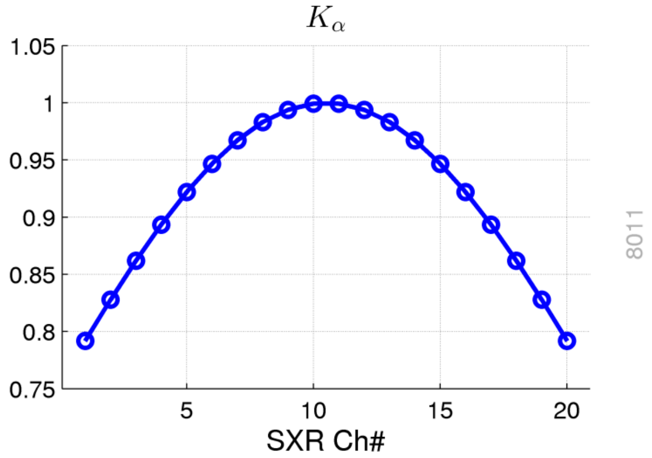

Figure 9-3: Soft X-Ray Slit Attenuation (K_α) by Channel

* * *

* * *